

Review

Recent Advances of Photocatalytic Hydrogenation of CO₂ to Methanol

Gajanan Y. Shinde , Abhishek S. Mote  and Manoj B. Gawande * 

Department of Industrial and Engineering Chemistry, Institute of Chemical Technology, Mumbai-Marathwada Campus, Jalna 431203, India; chy20gy.shinde@stumarj.ictmumbai.edu.in (G.Y.S.); moteabhishek298@gmail.com (A.S.M.)

* Correspondence: mb.gawande@marj.ictmumbai.edu.in

Abstract: Constantly increasing hydrocarbon fuel combustion along with high levels of carbon dioxide emissions has given rise to a global energy crisis and environmental alterations. Photocatalysis is an effective technique for addressing this energy and environmental crisis. Clean and renewable solar energy is a very favourable path for photocatalytic CO₂ reduction to value-added products to tackle problems of energy and the environment. The synthesis of various products such as CH₄, CH₃OH, CO, EtOH, etc., has been expanded through the photocatalytic reduction of CO₂. Among these products, methanol is one of the most important and highly versatile chemicals widely used in industry and in day-to-day life. This review emphasizes the recent progress of photocatalytic CO₂ hydrogenation to CH₃OH. In particular, Metal organic frameworks (MOFs), mixed-metal oxide, carbon, TiO₂ and plasmonic-based nanomaterials are discussed for the photocatalytic reduction of CO₂ to methanol. Finally, a summary and perspectives on this emerging field are provided.

Keywords: photocatalysts; nanomaterials; CO₂ reduction; methanol; photocatalytic CO₂ conversion



Citation: Shinde, G.Y.; Mote, A.S.; Gawande, M.B. Recent Advances of Photocatalytic Hydrogenation of CO₂ to Methanol. *Catalysts* **2022**, *12*, 94. <https://doi.org/10.3390/catal12010094>

Academic Editor: Vincenzo Vaiano

Received: 6 December 2021

Accepted: 11 January 2022

Published: 14 January 2022

Publisher's Note: MDPI stays neutral with regard to jurisdictional claims in published maps and institutional affiliations.



Copyright: © 2022 by the authors. Licensee MDPI, Basel, Switzerland. This article is an open access article distributed under the terms and conditions of the Creative Commons Attribution (CC BY) license (<https://creativecommons.org/licenses/by/4.0/>).

1. Introduction

Today's global issues and challenges include the energy crisis and environmental concerns [1]. Carbon dioxide comes primarily from the combustion of carbon sources such as fossil fuels and other natural sources. Developing renewable energy technologies to reduce pollutant emissions has become a significant area of research for the development of a sustainable planet.

In light of this, various advanced nanomaterials for CO₂ reduction have been reported, including alkali hydroxide [2,3], CuNi@g-C₃N₄/TiO₂ [4,5], Pd50-Ru50/MXene [6,7], CoSA-Ti₃C₂T_x [8,9], CuSAs/TCNFs carbon nanofibers [10], and copper selenide (Cu₂xSe(y) nanocatalysts) [11]. Gawande and his co-workers recently reviewed advanced Ag-based nanomaterials used for various photocatalytic applications, including CO₂ hydrogenation processes [12]. One promising approach to addressing issues related to climate change and the energy crisis is photocatalytic CO₂ reduction into value-added chemicals. Photocatalysis is considered to be a promising method for CO₂ conversion into valuable products, such as methanol, methane, formaldehyde, ethanol, and higher hydrocarbons [13]. Photosynthesis is an ideal method for effectively resolving issues relating to energy and the environment by reducing CO₂ into value-added chemicals and fuels [14]. The photocatalytic performance of a photocatalyst is highly dependent upon its electronic band structure and bandwidth energy. For an effective photocatalyst, the bandgap energy must be less than 3 eV to expand the light absorption in the visible area and use solar power efficiently. To date, a variety of photocatalysts including P- and F-co-doped carbon nitride (PFCN) [15], RuSA-mC₃N₄ [16], Cu-ZIF [17,18], single Cu₂O particle [19,20], g-C₃N₄-TiO₂ [21], (Pd/Pt)SA/g-C₃N₄ [22], O-doped g-C₃N₄ (OCN-Tube) [23], Cu-TiO₂ [24], Ni-nanocluster loaded on TiO₂ (Ni/TiO₂[V_o]) [25], aerogel flow-reactor [26], porous-g-C₃N₄/TiO₂-nanotube [27–29], carbon-doped TiO₂ [30–32], RGO-NH₂-MIL-125(Ti) [33], Cu porphyrin-based MOF [34],

Zn₂GeO₄/ZIF-8 nanocomposite [35,36], TZZ-TA-CMP [37], graphene quantum dots [38] and In₂O₃-CuO [39] have been reported for photocatalytic CO₂ reduction to valuable chemicals. Figure 1 indicates that the interest of researchers is continuously growing in the field of “Photocatalytic reduction of CO₂ to methanol”. In the last decade, there has been a significant increase in the publication of research articles. Recently, carbon, TiO₂, MOFs, and mixed-metal-oxide-based supporting materials have been utilized for photocatalytic hydrogenation of carbon dioxide into methanol. In this context, highly efficient solar-convertible materials to be reserved into chemicals are desired.

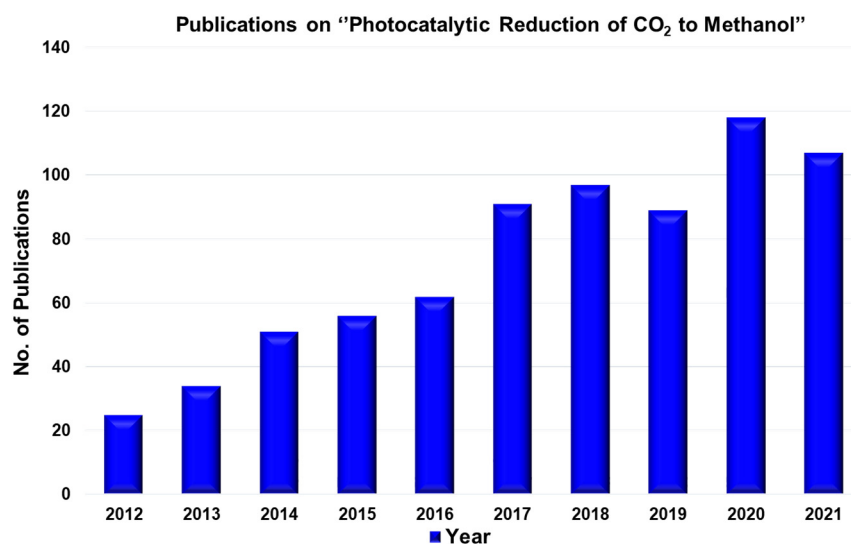


Figure 1. The number of publications for the keyword search “Photocatalytic reduction of CO₂ to methanol” as found in Web of Science (dated: 12 November 2021).

Due to its role as a greenhouse gas, the conversion of CO₂ to alternative chemicals has enabled many options. However, CO₂ is highly thermodynamically stable, which means that converting it into valuable chemicals requires a large amount of energy. A promising photo-reduced product of CO₂ is methanol. Methanol has multiple applications, including fuel transportation, biodiesel transesterification, and electricity generation [40–42]. The CO₂ conversion to methanol is a highly suitable method for reducing CO₂ emissions into the atmosphere. Methanol is greener than gasoline and has a high energy density. In addition to being a feasible clean fuel, methanol is also an important feedstock for chemical industries. The internal combustion engines can directly use it if stored at atmospheric pressure (atm P) due to its high octane number [43,44]. In light of all the above advantages of methanol, we examine the various strategies to enhance the photocatalytic CO₂ conversion to CH₃OH using carbon-based, TiO₂ based, MOFs based, mixed metal-oxide, and plasmonic-based photocatalysts.

2. Scope and Focus of This Review

CO₂ emissions are one of the greatest environmental concerns globally today. It is extremely necessary to convert this atmospheric CO₂ into valuable fuel or chemicals through catalysis. Photocatalysis is one of the ideal paths for CO₂ conversion into value-added products.

There has not been a review on photocatalytic selective hydrogenation of CO₂ to methanol yet. Though there are some reviews on CO₂ reduction into value-added chemicals reported, none of these reviews focused solely on methanol [43–54]. Thus, in this review, we highlighted the photocatalytic CO₂ reduction to selectively solar fuel such as methanol by using photoactive supporting materials, including carbon, TiO₂, MOF, mixed metal-oxide, and plasmonic based photocatalysts (Figure 2). We believe that a detailed overview of the catalytic performance of various photocatalysts for CO₂ reduction to methanol would

be useful to a broad community of scientists with interests in nanotechnology, materials chemistry, inorganic chemistry, organic chemistry, and chemical engineering.

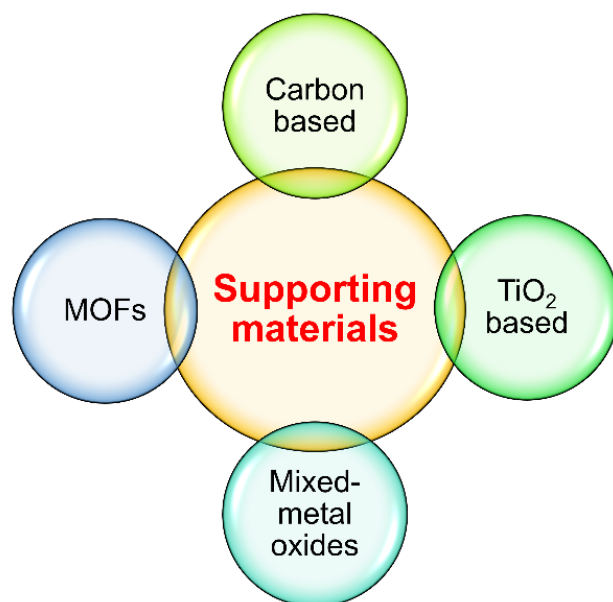


Figure 2. The supporting materials used in photocatalytic CO₂ reduction to fuels.

3. Applications

Photocatalytic CO₂ reduction is a promising method for converting CO₂ into valuable fuels and chemicals by utilising solar energy. An everyday variety of products utilize methanol as a chemical building block, such as paints, plastics, and construction materials. In this section, a variety of photocatalysts for CO₂ reduction to methanol are included, including MOF-based, mixed-metal oxide-based, carbon-based, TiO₂-based and plasmonic-based photocatalysts.

3.1. Photocatalyst Based on MOFs

The metal–organic framework (MOF) is a hybrid (inorganic–organic) crystalline porous material that consists of metal ions surrounded by organic linkers. Due to an internal hollow structure, it has a remarkably large internal surface area, since the metal ions serve as nodes that bind the linker arms together [55]. In contrast to other porous materials, MOFs exhibit unparalleled structural diversity—atomic structural uniformity, uniform pore structures, tunable porosity, as well as flexibility in network topology, and chemical utility. MOFs' cage-like structure is currently being exploited in numerous fields, including purification, gas separation and storage, liquid separation, sensing, gas storage, and catalysis [49]. The various types of MOF-based photocatalysts, such as MOF-based, MOF composites, MOF-derived, MOFs as support, and single-site MOFs, are employed for the reduction of CO₂.

In recent years, MOF-based materials for photoreduction of CO₂ have attracted significant research interest [50]. MOF materials are easily designed with convenient metallic sites, specific heteroatoms, and an orderly structure of functional organic ligands [54]. They can efficiently increase the efficiency of photocatalytic activity and electron–hole separation. MOF porosity can help to expose channels for reactant adsorption and more active sites, thus resulting in an excellent catalytic performance. This can increase the efficiency of charge transfer and solar power while inhibiting the recombination of photo-induced electrons. Based on the above merits, the researchers attempt to use various MOFs for the photocatalytic reduction of CO₂.

MOFs have porous and channel structures that provide anchored centres for photocatalysis, giving them their structural and functional characteristics. Wang et al. reported

composites ($\text{Cd}_{0.2}\text{Zn}_{0.8}\text{S}/\text{UiO-66-NH}_2$) with various UiO-66-NH_2 compositions via the solvothermal method, which is used for CO_2 photoreduction and hydrogen evaluation under visible light [55]. The electron microscopic (TEM/HR-TEM) images of CZS/UN20 confirmed that $\text{Cd}_{0.2}\text{Zn}_{0.8}\text{S}$ NPs were evenly distributed on the surface of the UiO-66NH_2 cubes, and the lattice spacing (0.313 nm), which corresponds to the (111) plane of $\text{Cd}_{0.2}\text{Zn}_{0.8}\text{S}$ (Figure 3a,b). The composite ($\text{Cd}_{0.2}\text{Zn}_{0.8}\text{S}/\text{UiO-66-NH}_2$) showed the largest photocurrent density, implying effective photo-generated charge transfer (between $\text{Cd}_{0.2}\text{Zn}_{0.8}\text{S}$ and UiO-66-NH_2), which is reliable for improved photocatalytic performance (Figure 3c). The UiO-66-NH_2 content significantly influences the photoactivity of $\text{Cd}_{0.2}\text{Zn}_{0.8}\text{S}$. The CZS@UN20 sample shows the higher methanol evolution rate among the as-prepared samples ($6.8 \mu\text{mol h}^{-1} \text{g}^{-1}$) under irradiation of visible light; it was larger (3.4 times) compared to pure $\text{Cd}_{0.2}\text{Zn}_{0.8}\text{S}$ (Figure 3d). Because of the transfer and charge separation (between $\text{Cd}_{0.2}\text{Zn}_{0.8}\text{S}$ and UiO-66-NH_2), the photo-induced electrons absorbed by these materials could be transferred over the surface for the reduction of CO_2 . Apart from photocatalytic performance, the lifetime of the catalyst is very important. Furthermore, the photocatalyst ($\text{Cd}_{0.2}\text{Zn}_{0.8}\text{S}/\text{UiO-66-NH}_2$) showed excellent stability after four recycles in the system of photoreduction CO_2 (Figure 3e). A plausible interface electron transfer behaviour and a related mechanism of photocatalytic CO_2 reduction were demonstrated in Figure 3f.

The Z-scheme heterojunction has a high electron-hole pair separation efficiency and redox ability and a broad light response range. The Z-scheme heterojunction is a wonderful alternative for converting CO_2 into value-adding compounds because of the advantages listed above. The artificial Z-scheme photocatalyst is typically made up of two connected semiconductor photocatalysts: one for oxidation and the other for reduction [56]. The Z-scheme gets its name from the fact that it connects the two photosystems in a fashion that looks like the letter "Z". In particular, the engineered Z-scheme direct photocatalysts that mimic the natural photosynthetic system provide a number of advantages, including improved light uptake, spatially separated reductive and oxidative active sites, and well-preserved strong redox capacity. Furthermore, photogenerated separation was made possible by the heterojunction at the interfaces, which boosted the charge participation in catalysed conversion reactions [57]. Heterojunctions (Z-scheme) are an effective way to isolate photogenerated electron holes and improve photocatalytic activity in semiconductors. On the other hand, heterojunction-based MOFs are rarely documented. In a similar context, Liu et al. have recently designed a Z-scheme O-ZnO/rGO/UiO-66-NH₂ (OZ/R/U) heterojunction that was obtained by pairing UiO-66-NH₂ and rGO (reduced graphene oxide) with O-ZnO (oxygen-poor) by a facile solvothermal method [58]. The SEM and TEM images of the OZ/R/U catalyst displayed that the UiO-66-NH₂ and O-ZnO were well dispersed over the rGO NS with close contact (Figure 4a,b). The OZ/R/U catalyst has a much higher photocurrent intensity than the OZnO and UiO-66-NH₂ catalysts. As a result, it confirms the high charge transfer and separation ability of the OZ/R/U (Figure 4c). The optimal rGO content was 1.5 wt% for the photoactivity of the composite OZnO/rGO/UiO-66-NH₂ photocatalyst (Figure 4d). Under visible light irradiation, the ternary photocatalyst demonstrated excellent photocatalytic performance for CO_2 reduction into methanol and formic acid, as well as good stability. The results showed that this ternary composite could effectively reduce CO_2 to HCOOH and CH_3OH and that activity was far better than ZnO/rGO/UiO-66-NH₂ and O-ZnO/UiO-66-NH₂. Under visible light irradiation, the yield of HCOOH and CH_3OH over the ternary composite (O-ZnO/rGO/UiO-66-NH₂) achieved 6.41 and $34.83 \mu\text{mol g}^{-1} \text{h}^{-1}$, respectively (Figure 4e). The photoinduced electrons on the CB of O-ZnO are transferred to the VB of UiO-66-NH₂ through rGO and combined with the photoinduced holes, resulting in the accumulation of electrons on the CB of UiO-66-NH₂ and the accumulation of holes over the VB of O-ZnO. The CB level of UiO-66-NH₂ is more negative than the reduction potential of CO_2 . The electrons accumulated over CB of UiO-66-NH₂ can readily reduce CO_2 to methanol. This Z-scheme charge transfer process of the above two semiconductors can reduce the rate of recombination of photogenerated charge carriers while maintaining the photogenerated electrons' high reduction capacity at

more negative CB of UiO-66-NH₂ and the strong oxidation capacity of the photoinduced holes over more positive VB of O-ZnO. This Z-scheme photocatalytic system improved charge separation efficiency by transferring electrons from the CB of O-ZnO to the rGO NS and then recombining those electrons to holes in the VB of UiO-66-NH₂ (Figure 4f). This boosted composite photocatalyst activity was assigned to the development of a photocatalytic system (Z-scheme), which inhibits photogenerated charge carriers' recombination, while maintaining the high reduction capacity of UiO-66-NH₂ and the strong oxidizing ability of O-ZnO (Figure 4f).

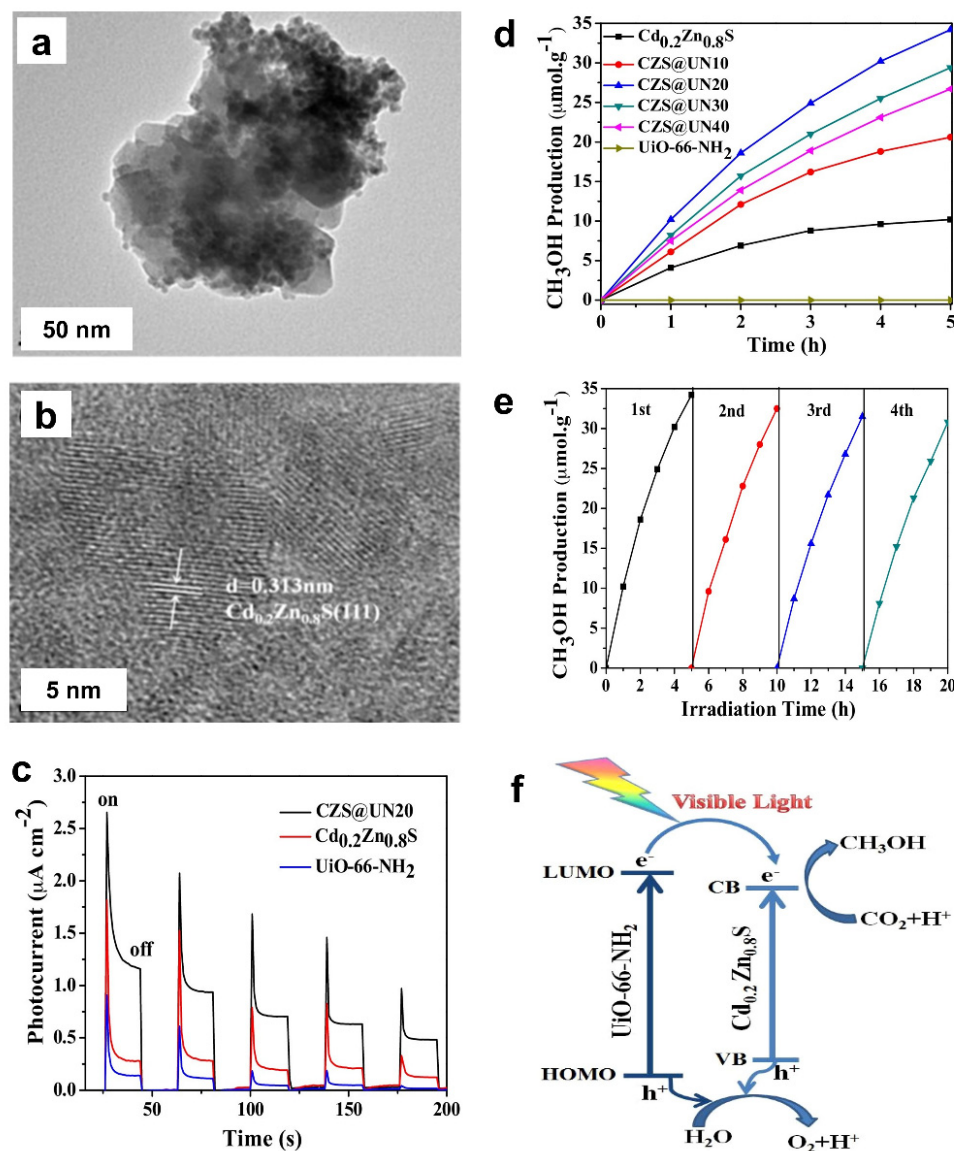


Figure 3. (a,b) TEM and HR-TEM images of CZS@UN20; (c) Photocurrent spectra; (d) Methanol production; (e) Cycle runs for reduction of CO₂ over the CZS@UN20 photocatalyst; (f) Mechanism for photocatalytic (visible light) CO₂ reduction. Reproduced from [55] with permission.

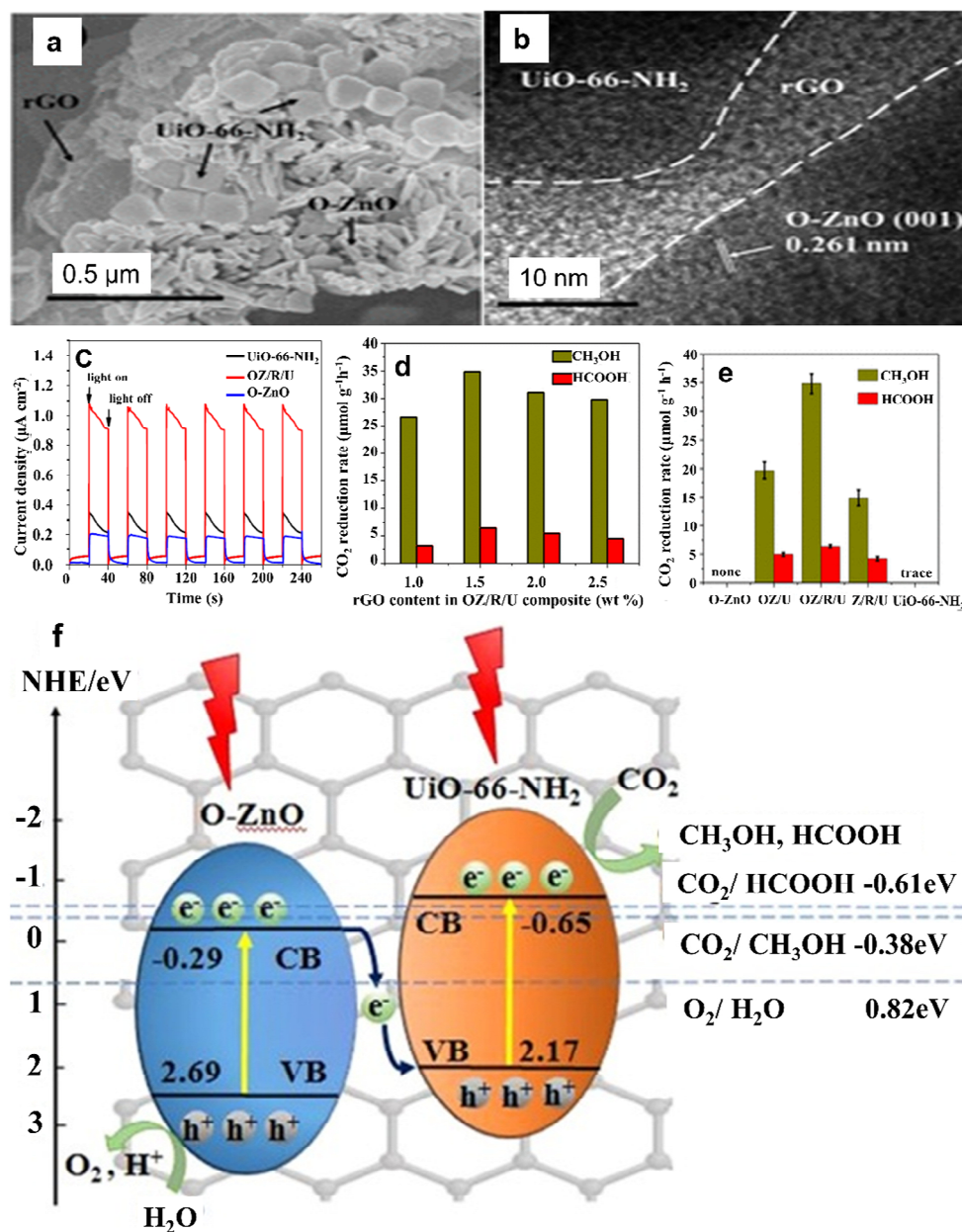


Figure 4. (a,b) SEM and HR-TEM images of OZ/R/U catalyst; (c) Photocurrent spectra; (d) The impact of rGO on photoactivity of the ternary composite (OZ/R/U); (e) Photocatalytic activity; (f) Photocatalytic mechanism over O-ZnO/rGO/UiO-66-NH₂ composites. Reproduced from [58] with permission.

The copper single-atoms (Cu_{SA}) on the UiO-66-NH₂ support (Cu_{SA}@UiO-66-NH₂) have been developed for photoreduction of CO₂ into liquid fuels in water medium (Figure 5a) [59] under visible-light irradiation. The morphology of the Cu_{SA}@UiO-66-NH₂ photocatalyst was studied by HR-TEM and AC-STEM analysis, which clearly verified the occurrence of a Cu single-atom catalyst marked with red circles (Figure 5b–d). The images of elemental mapping of (Cu_{SA}@UiO-66-NH₂), furthermore, demonstrated that the atoms N, C, O, Cu and Zr are uniformly dispersed on the support (Figure 5e). Remarkably, it was observed that the photocurrent density of Cu_{SA}@UiO-66-NH₂ was more than UiO-66-NH₂, and the Cu_{NPs}@UiO-66-NH₂ catalysts showed that a larger number of carriers were produced under visible light illumination (Figure 5f). Remarkably, the developed Cu_{SA}@UiO-66-NH₂ reached the solar-induced CO₂ conversion to ethanol and methanol with an evolution

rate of about $4.22 \mu\text{mol h}^{-1} \text{g}^{-1}$ and $5.33 \mu\text{mol h}^{-1} \text{g}^{-1}$, respectively. The yields were significantly higher as compared to pure counterparts (Figure 5g).

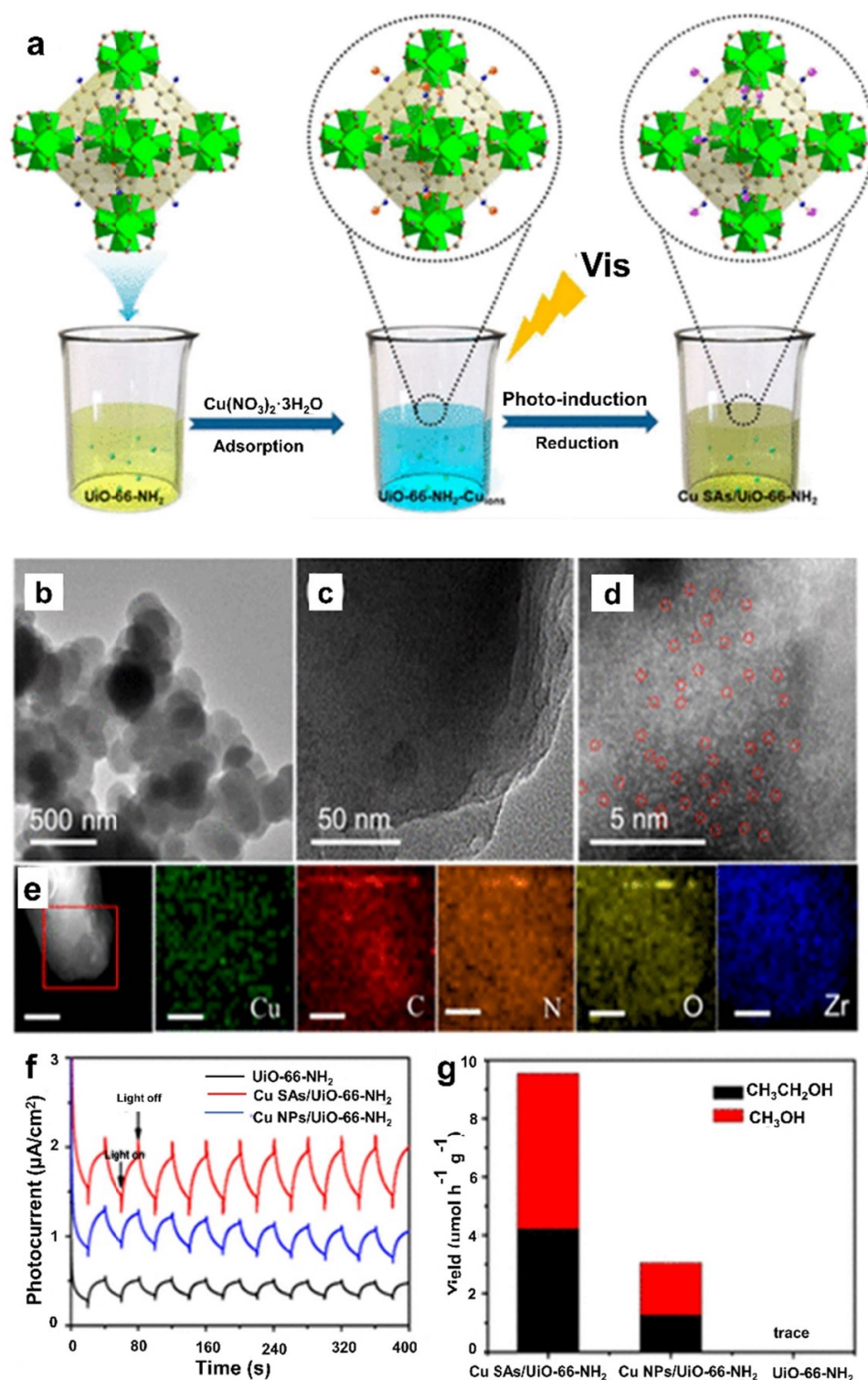


Figure 5. (a) Schematic representation for the synthesis of (Cu_SA@UiO-66-NH₂) photocatalyst; (b,c) The (TEM and HR-TEM) images of Cu_SA@UiO-66-NH₂ photocatalyst; (d) AC-STEM image of Cu_SA@UiO-66-NH₂; (e) EDS mapping; (f) Photocurrent spectra; (g) Photocatalytic activity. Reproduced from [59] with permission.

Liu et al. developed (ZIF-8/g-C₃N₄) composites by developing various compositions of nanoclusters of ZIF-8 over the surface of g-C₃N₄ [60]. The ZIF-8 nanoclusters were deposited over g-C₃N₄ nanotubes (NT); the overall tubular morphology remained the same (Figure 6a). Additionally, some nanoparticles protruded from the tube wall of g-C₃N₄ nanotubes. The corresponding TEM image indicated that the ZIF-8 was effectively inserted on the surface of the g-C₃N₄ NT (Figure 6b). After ZIF-8 surface grafting, charge separation and transfer efficiency were retarded. Further confirmation of this conclusion came from the photoelectrochemical measurements. Among the three samples, a TCN sample achieved the highest stable photocurrent value, indicating the rapid charge separation (Figure 6c,d). Due to the incorporation of ZIF-8 nanoclusters, ZIF-8@g-C₃N₄ composites could adsorb more CO₂ than the g-C₃N₄ NT without compromising light absorption ability. The (ZIF-8/g-C₃N₄) composites had improved photocatalytic functioning for the reduction of CO₂ due to the higher charge separation efficacy and CO₂ capture ability of ZIF-8 from the g-C₃N₄ NT, where the highest methanol evolution rate arrived at 0.75 mmol h⁻¹ g⁻¹ under the ZIF-8/g-C₃N₄ composite (Figure 6e). The methanol production rate for bulk g-C₃N₄ and g-C₃N₄ NT was 0.24 and 0.49 mmol h⁻¹ g⁻¹ respectively, under similar conditions. However, the methanol was not produced on pristine ZIF-8 nanocrystals. Remarkably, the number of grafted ZIF-8 nanoclusters was critical for the conversion of ZIF-8 and synergetic nanostructural patterns. By combining nanostructure semiconductor and MOF grafts, the ZIF-8/g-C₃N₄ photocatalyst exhibited an enhanced capacity of CO₂ adsorption, light-harvesting ability, and charge separation efficiency; it therefore, exhibited an excellent increment in effective photocatalytic methanol generation. Typically, a higher CO₂ adsorption capability accompanies a greater efficiency of photocatalytic CO₂ reduction for a semiconductor photocatalyst.

In a membrane reactor, Maina et al. demonstrated the controlled incorporation of TiO₂ nanoparticles and Cu^{II}-doped TiO₂ nanoparticles over ZIF-8 films via the rapid thermal deposition (RTD) method (Figure 7a) [61]. The presence of TiO₂ NPs in the MOF matrix was emphasized with the red square (Figure 7c). Under UV irradiation, the Cu-TiO₂@ZIF-8 hybrid film exhibited powerful photocatalytic activity. The results indicate that, compared with only the quantity generated by pure ZIF-8 film single, the yields of CH₃OH and CO raised by 50% and 188%, respectively (Figure 7d). Furthermore, when Cu@TiO₂ nanoparticles are loaded on MOF, the photocatalytic CO₂ reduction to CO and CH₃OH is considerably enhanced (Figure 7e). When the loading of Cu@TiO₂ nanoparticles was 7 µg, the Cu-TiO₂@ZIF-8 displayed excellent catalytic efficacy. Compared to the pure ZIF-8 film, CO and CH₃OH yields were 23.3% and 70% respectively. This is attributed to a synergistic effect caused by semiconductor NPs' ability to generate photogenerated electrons under light illumination and the CO₂ adsorption potential of MOFs.

In 2018, Cardoso et al. prepared a MOF-based Ti/TiO₂NT-ZIF-8 photocatalyst by growing films of ZIF-8 over Ti@TiO₂ nanotube electrodes through a layer-by-layer method (Figure 8a) [62]. Figure 8b shows the addition of ZIF-8 composites to the TiO₂ NTs. Figure 8c displays the image captured by TEM for Ti/TiO₂NT-ZIF-8: ZIF-8 nanoparticles can be observed between and within TiO₂ nanotubes. The photo-electrocatalytic CO₂ reduction by (Ti/TiO₂NT-ZIF-8) electrodes was executed in sodium sulphate saturated with CO₂ at a constant potential (+0.1 V) under UV-visible light illumination. Notably, 0.7 mmol/L of methanol and 10 mmol/L of ethanol were generated in 3 h (Figure 8d). Because of the lack of ZIF-8 films, the Ti⁴⁺ species in Ti@TiO₂NT may have a lower ability for CO₂ absorption (Figure 8e).

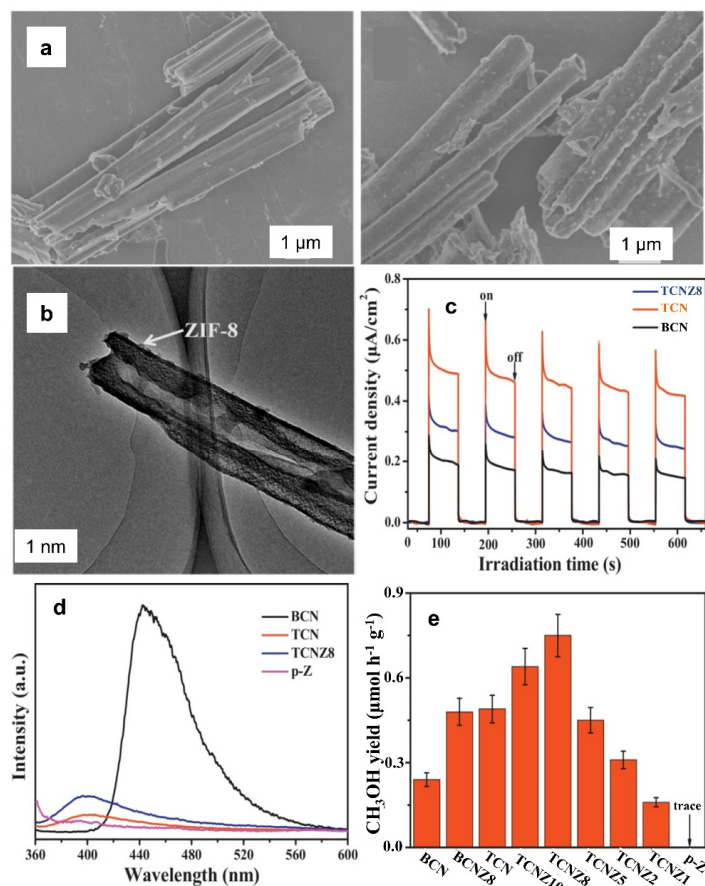


Figure 6. (a,b) FESEM and TEM images of TCNZ8 sample (ZIF-8/g-C₃N₄ photocatalyst); (c) Photocurrent spectra; (d) The steady-state PL spectra; (e) Photocatalytic activity. Reproduced from [60] with permission.

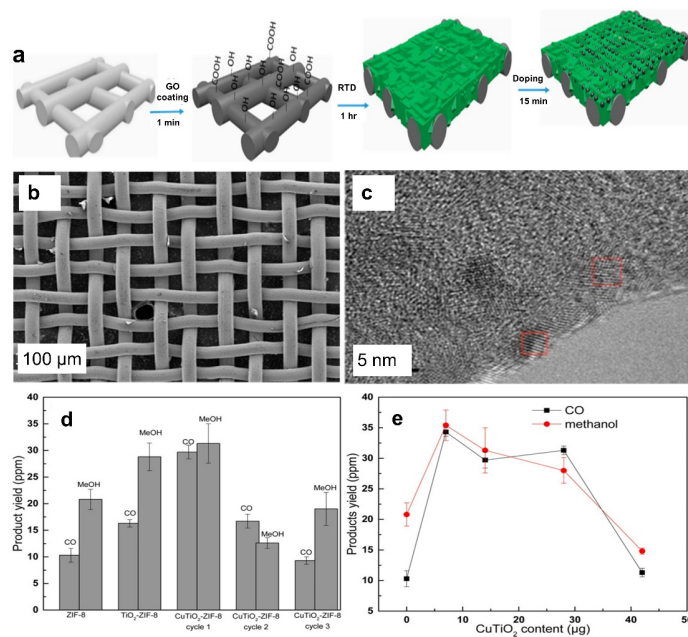
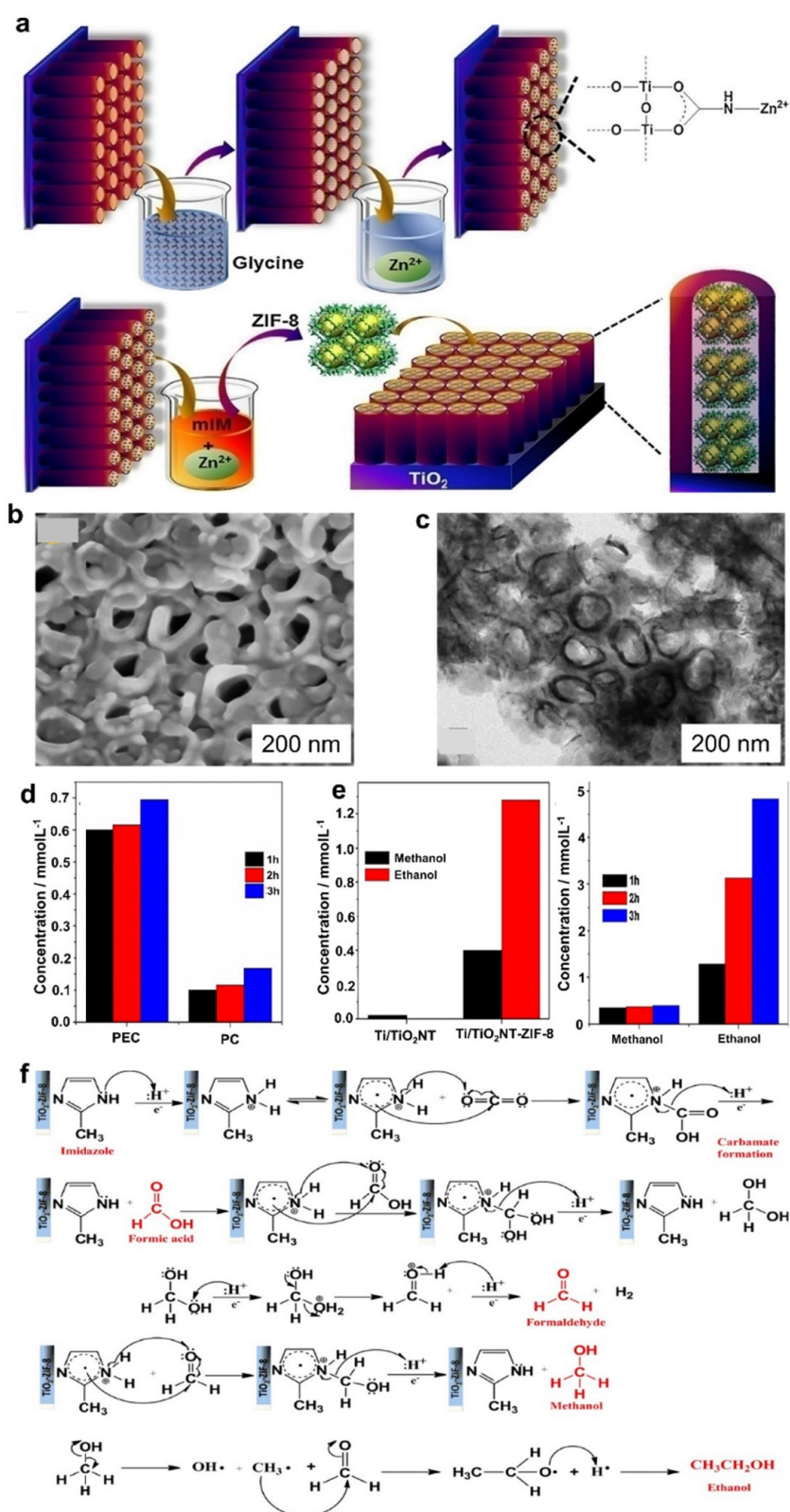


Figure 7. (a) A schematic representation for the synthesis of Cu-TiO₂/ZIF-8 membranes; (b) SEM image of porous substrate; (c) The high-resolution (HR-TEM) image of the TiO₂@ZIF-8 hybrid; (d) Effect of Cu-TiO₂ nanoparticle loading on product yields; (e) The impact of membrane content on yield of product. Reproduced from [61] with permission.



As a consequence of the interaction between Cu/ZnO_x nanoparticles and their ligands and Zr₆ SBUs, these ultra-small well-mixed NPs do not agglomerate as much and do not undergo phase separation. The Cu/ZnO_x@MOF catalysts produce extremely higher activity with yield (2.59 g MeOH kg Cu⁻¹ h⁻¹), and higher selectivity for the CO₂ hydrogenation to obtain methanol, and strong stability for over 100 h. The catalyst was prepared by the in situ reduction of post-synthetic metalized UiO-bpy (Figure 9a). The ideal precatalyst structure of Zn@UiO-bpy-Cu via post-synthetic Cu co-ordination to bpy is shown in Figure 9b. As shown in Figure 9c, the CuZn@UiO-bpy has enriched sites that enhance the yield of methanol. The Cu and ZnO_x combine well to form Zn and Zr, which leads to improved hydrogenation of CO₂. The STEM-HAADF images of ultrasmall Cu/ZnO_x and CuZn@UiO-bpy catalyst clearly showed the Cu and Zn were uniformly dispersed and mixed across the entire MOF particle and nanoparticles of 0.5–2.0 nm in size (Figure 9d,e). The UiO-bpy proved to have an effective selectivity for methanol production (Figure 9f).

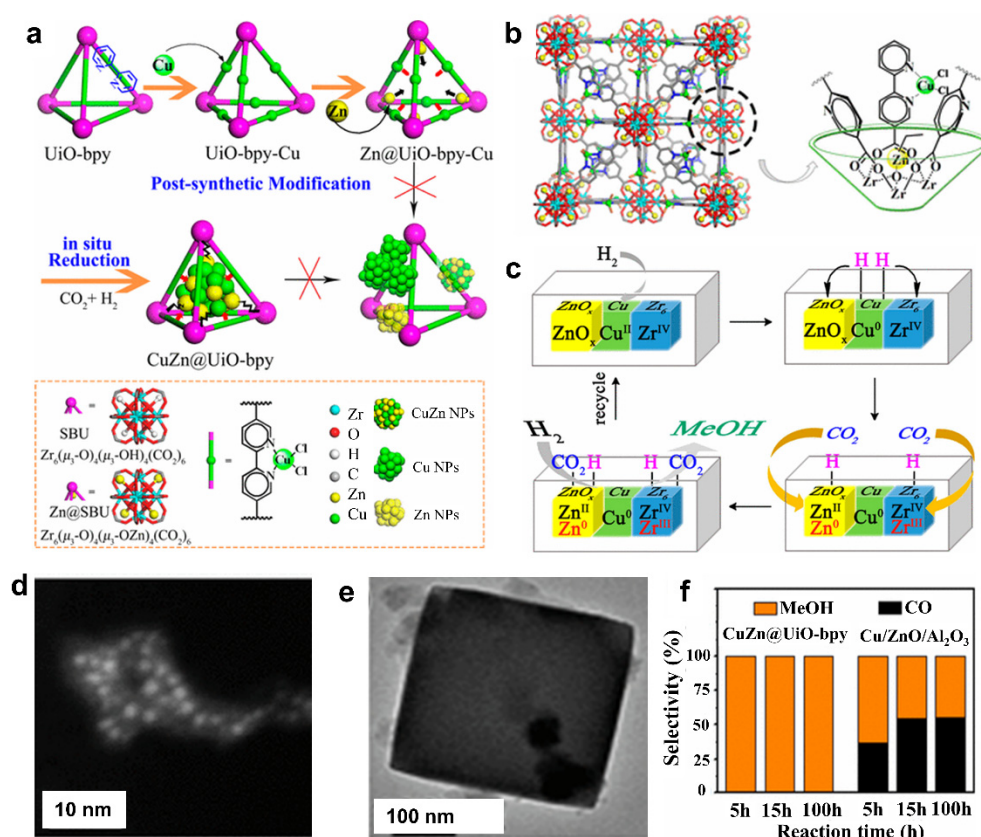


Figure 9. (a) The preparation of CuZn@UiO-bpy catalyst; (b) The precatalyst structure (Zn@UiO-bpy-Cu); (c) Active sites of MOFs; (d,e) STEM-HAADF images of ultrasmall Cu/ZnO_x and CuZn@UiO-bpy catalyst (f) Product selectivity. Reproduced from [63] with permission.

It was crucial to enhance the stability of metal-oxide QDs for reaction patterns containing H₂O so that they could be employed in photocatalytic CO₂ reduction. Recently, Li et al. designed the (g-C₃N₄/CuO@MIL-125(Ti)) photocatalyst for the reduction of CO₂ with the proximity of H₂O by encapsulating CuO quantum dots with pores of MOFs of MIL-125 (Ti) via a complexation-oxidation method (Figure 10a) [64]. In aqueous reaction systems, the photocatalyst displays significantly enhanced stability due to the protection offered by the MIL-125(Ti) framework. Because of the close contact between the CuO QDs and the Ti active site in MIL-125 (Ti), electron transfers between the confined CuO QDs and the Ti active site were observed (Figure 10b). The presence of water greatly increases the photocatalytic activity of g-C₃N₄/CuO@MIL-125(Ti) composites for the photoreduction of CO₂. Among the prepared catalysts, the resultant 2.5% g-C₃N₄/1%CuO@MIL-

125(Ti) photocatalyst performed better for photocatalytic reduction of CO_2 to CH_3OH , CO , CH_3CHO , and $\text{CH}_3\text{CH}_2\text{OH}$, implying water (reductant), with yields of 997.2, 180.1, 531.5, and 1505.7 $\mu\text{mol/g}$, respectively (Figure 10c). Figure 10d–g depicts the structural morphologies of the 2.5% $\text{g-C}_3\text{N}_4$ /1% CuO@MIL-125(Ti) photocatalyst. This study developed an efficient method for enhancing charge separation efficiency and stability of metallic-oxide QD-adapted photocatalyst. Furthermore, MIL-125(Ti), due to its high specific surface area and porous structure, provides an encapsulating structure for CuO QDs to prevent aggregation and provides excellent stability and recyclability. Moreover, the unique heterostructure of the composite ensures high light absorption and efficient electron transport from $\text{g-C}_3\text{N}_4$ nanosheets and MIL-125(Ti) to QDs as well. The recent research progress of MOF-based materials/photocatalysts for photocatalytic reduction of CO_2 is summarised in Table 1.

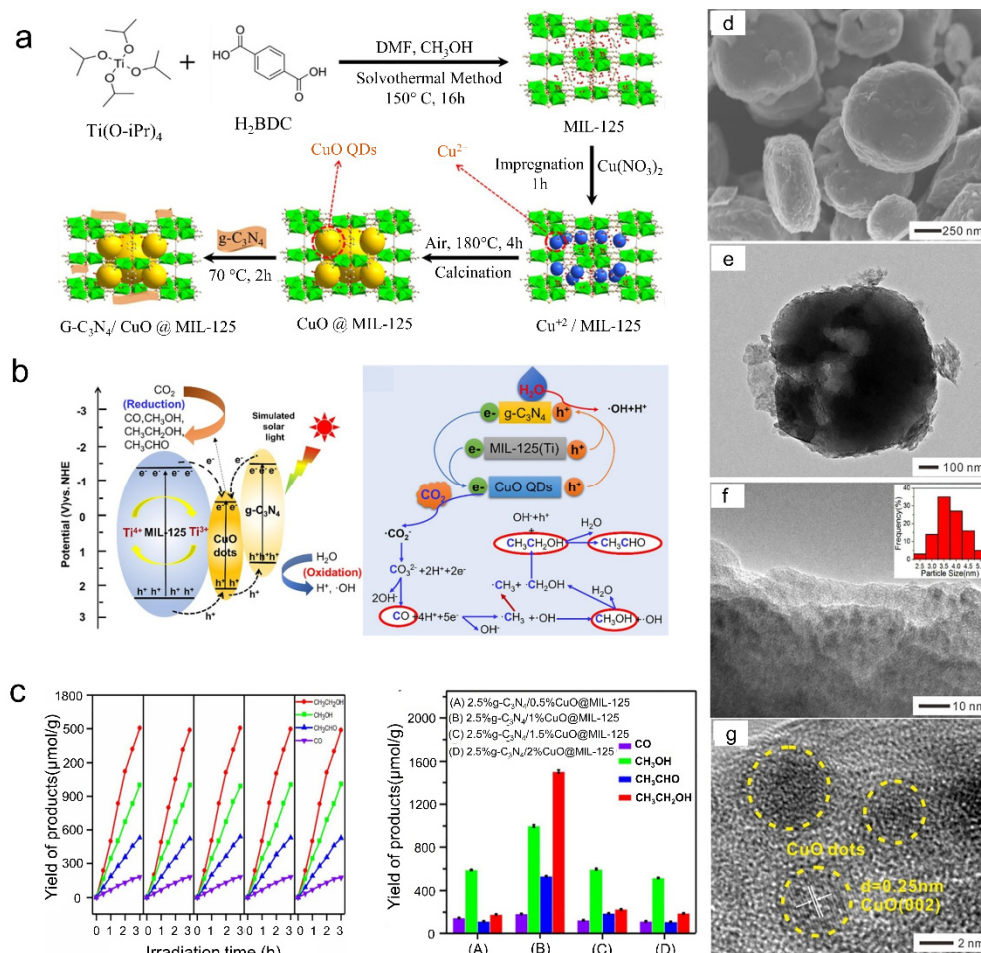


Figure 10. (a) The preparation of $\text{g-C}_3\text{N}_4/\text{CuO@MIL-125(Ti)}$ composite photocatalyst; (b) CO_2 reduction mechanism; (c) Photocatalytic stability and product selectivity; (d–g) The morphological analysis of $\text{g-C}_3\text{N}_4$ /1% CuO@MIL-125(Ti) catalyst with (SEM/TEM/HR-TEM) images. Reproduced from [64] with permission.

Table 1. Reported MOF-based photocatalysts for reduction of CO₂ to fuels.

Photocatalyst	Light Source	Method	Products Yield (μmol h ⁻¹ g ⁻¹)	Proton Donor/ Reaction Reagent	Year	Ref.
Cu-porphyrin MOFs	Visible		CH ₃ OH (262.6)	TEOA	2013	[34]
Cu (II) ZIF	Visible	Hydrothermal	CH ₃ OH (1712.7)	H ₂ O	2013	[65]
Zn ₂ GeO ₄ /ZIF-8	UV	Hydrothermal	CH ₃ OH (0.22)	H ₂ O	2013	[35]
Cd _{0.2} Zn _{0.8} S@UiO-66-NH ₂	Visible	Solvothermal method	CH ₃ OH (6.8)	H ₂ O	2017	[55]
g-C ₃ N ₄ /ZIF-8	300 W Xe lamp	In situ heterogeneous deposition method	CH ₃ OH (0.75)	H ₂ O	2017	[60]
Cu/ZnO _x MOFs	-	Solvothermal	CH ₃ OH (2.59)	H ₂	2017	[63]
Cu-TiO ₂ ZIF-8	UV	Rapid thermal deposition (RTD)	CH ₃ OH, CO	TEOA	2017	[61]
TiO ₂ ZIF-8	UV-Visible	Layer-by-layer process	CH ₃ OH, CH ₃ CH ₂ OH	Na ₂ SO ₄	2018	[62]
Zn-Ni bimetallic MOF		Calcination/Thermal	CH ₃ OH		2018	[66]
2Cu-ZIF-8N ₂	Visible	Hydrothermal	CH ₃ OH (35.82)	Na ₂ SO ₃	2018	[67]
Cu-porphyrin-Ti-MCM-48	Visible	Impregnation	CH ₃ OH (297)	Na ₂ SO ₃	2018	[68]
O-ZnO/rGO/UiO-66-NH ₂		Solvothermal	CH ₃ OH (34.85), HCOOH (6.41)	TEOA	2019	[58]
rGO-NH ₂ -MIL-125(Ti)	Visible		CH ₃ OH	TEOA	2020	[33]
g-C ₃ N ₄ /CuO@MIL-125(Ti)	Visible light	Complexation-oxidation method	CH ₃ OH, CO, CH ₃ CH ₂ OH, CH ₃ CHO		2020	[64]
Au _x @ZIF-67	Visible		CH ₃ OH (2.5), CH ₃ CH ₂ OH (0.5)		2020	[69]
Cu _{SA} @UiO-66 NH ₂	Visible		CH ₃ OH (5.33), CH ₃ CH ₂ OH (4.22)	TEOA	2020	[59]

3.2. Mixed-Metal-Oxide-Based Photocatalyst

Mixed metal oxides (MMOs), containing two or more types of metals and oxygen, have been broadly employed as photocatalysts for the reduction of CO₂. The semiconducting properties of their aqueous suspensions irradiated with visible light have been a prominent subject of research. Mixed metal oxide (MMO) is one of the most important photocatalysts, with features that differ from ordinary oxides in circumstances such as acid-base, redox, and surface area. These have been widely explored for several catalytic applications due to their excellent chemical-thermal stability compared to single oxides [70–72].

Transition and Non-Transition Metals

Singhal et al. reported Ni/InTaO₄ as supported catalysts for the CO₂ photoreduction to methanol under visible light irradiation by the facile sol–gel method. Loading of 1 wt% Ni on InTaO₄-produced methanol with a higher yield and slowed down recombination by reducing the bandgap slightly. The bandgap of InTaO₄ and Ni/InTaO₄ catalysts was noted at 2.6 eV and 2.54 eV, respectively. The SEM image shows the agglomerated nature of the catalyst, and EDX confirmed the existence of elements (In, Ta, O, and Ni). TEM displays the size of nanomaterials at 50–80 nm. The HR-TEM demonstrated the crystallinity of InTaO₄, which was a good match for the XRD pattern. XPS measurement of the catalyst showed

the presence of Ni and NiO due to four peaks at different binding energies. The catalyst displayed sharp diffraction peaks, indicating monoclinic InTaO_4 . The material crystalline phase is not altered by Ni loading [73]. Recently, the bimetallic oxide was derived from MOFs developed by Cheng et al. [74].

Kumar et al. proposed a highly efficient rGO-covered magnetically separable core-shell-structured microsphere photocatalyst ($\text{rGO@CuZnO@Fe}_3\text{O}_4$) for CO_2 reduction below visible light illumination (Figure 11a) [75]. In order to allow simultaneous CO_2 reduction and water oxidation, the semiconductor should have a wide bandgap. Neither Fe_3O_4 nor ZnO by themselves can convert CO_2 to methanol because electrons can only move from the valence band (VB) to conduction band (CB) under the influence of UV light. The morphology of the surface and core-shell structure of microspheres were examined by FE-SEM tomography. The structure of $\text{rGO@CuZnO@Fe}_3\text{O}_4$ remains the same after GO reduction to rGO (Figure 11b). The HR-TEM image clearly showed the 1D lattice plane at about 0.26 nm interplanar distance, corresponding to the (002) plane of ZnO . Additionally, the amorphous zone (0.64 nm thickness) related to rGO was visual (Figure 11c,d). The $\text{rGO@CuZnO@Fe}_3\text{O}_4$ catalyst has shown excellent catalytic activity for a methanol yield ($2656 \mu\text{mol g}^{-1}$) among the various catalysts prepared (Figure 11e). The advantages of this catalyst include a high yield of methanol, no sacrificial donor requirement, ease of recovery, and effective recycling (Figure 11f). The methanol yield increased with Cu loading from 0.25 to 1.0 wt%; however, the photocatalytic performance did not improve with a further increase in Cu content. The enhancement in the reduction in methanol yield due to Cu content can be attributed to the trapping of photo-generated electrons, which reduces the recombination process of electron holes (Figure 11g). This catalyst has a low price, higher electron mobility, and environmental preservation than ZnO . The large surface area and excellent charge-carrier mobility of rGO can lead to the development of a highly efficient, reusable photocatalyst for CO_2 reduction.

Gao et al. synthesized separate V_v-rich and V_v-poor o- BiVO_4 atomic layers with the thickness of a unit of a cell at the gram-scale using an intermediate lamellar hybrid approach (Figure 12a) [76]. The single-unit-cell o- BiVO_4 layers with a high content of vanadium vacancies (V_v) are high in the production of methanol ($398.3 \mu\text{mol g}^{-1} \text{h}^{-1}$) compared to atomic layers of V_v-poor o- BiVO_4 (Figure 12c). At the atomic level, a correlation between defect sites and photoreduction of CO_2 was investigated. A density-functional theory calculation shows that vanadium (V) vacancies introduce a new defect level and greater hole concentration around Fermi levels, resulting in enhanced electronic conductivity and photoabsorption (Figure 12b). The increased surface photovoltage of layers with vanadium voids is confirmed by the enhanced carrier lifetime of the o- BiVO_4 layers, which is shown through time-persistent fluorescence spectra.

Yu et al. prepared a novel efficient visible light 2D photocatalyst ($\text{Ti}_3\text{C}_2/\text{Bi}_2\text{WO}_6$ nanosheets) via in situ progress of ultrathin nanosheets of Bi_2WO_6 with a surface of Ti_3C_2 nanosheets (Figure 13a) [77]. The generation of the 2D/2D heterojunction was characterized by TEM studies; the results demonstrated the clean ultrathin nanosheets along with lucent features, nanoparticles of $\text{Ti}_3\text{C}_2@ \text{Bi}_2\text{WO}_6$ nanosheets, and the element composition and distribution (Figure 13b–d). The $\text{Ti}_3\text{C}_2@ \text{Bi}_2\text{WO}_6$ heterostructured hybrids with distinct atomic layers had much higher photoreduction activity than pure Bi_2WO_6 , with a 4.6 times higher overall yield of CH_3OH and CH_4 than pure Bi_2WO_6 (Figure 13g). Under solar light irradiation, photo-induced electrons are excited and jump from the VB to the CB of Bi_2WO_6 . The Bi_2WO_6 has a more negative CB potential compared to the EF of Ti_3C_2 with terminal -O; photoinduced electrons can then be transferred from Bi_2WO_6 to Ti_3C_2 via an ultra-thin layered heterojunction. The photo-induced electrons that have accumulated on the surface of Ti_3C_2 can then interact with the CO_2 molecules that have been adsorbed. The photo-induced electrons can be quickly transferred from the bulk of Bi_2WO_6 to the heterojunction interface up to the Ti_3C_2 surface because of the unique atomic layer 2D/2D heterostructure. Thus, a significant enhancement in the efficiency of photocatalytic CO_2 reduction was observed. This 2D photocatalyst possesses a high

contact area and a small distance of charge transport. As a result, electrons are efficiently transferred from the Bi_2WO_6 (photocatalyst) to the Ti_3C_2 (cocatalyst) (Figure 13h). The enhancement of photocatalytic functioning is due to excellent CO_2 adsorption ability and effective separation of charge carrier. The present work demonstrated that Ti_3C_2 nanosheets can be employed as effective cocatalysts for the photoreduction of CO_2 .

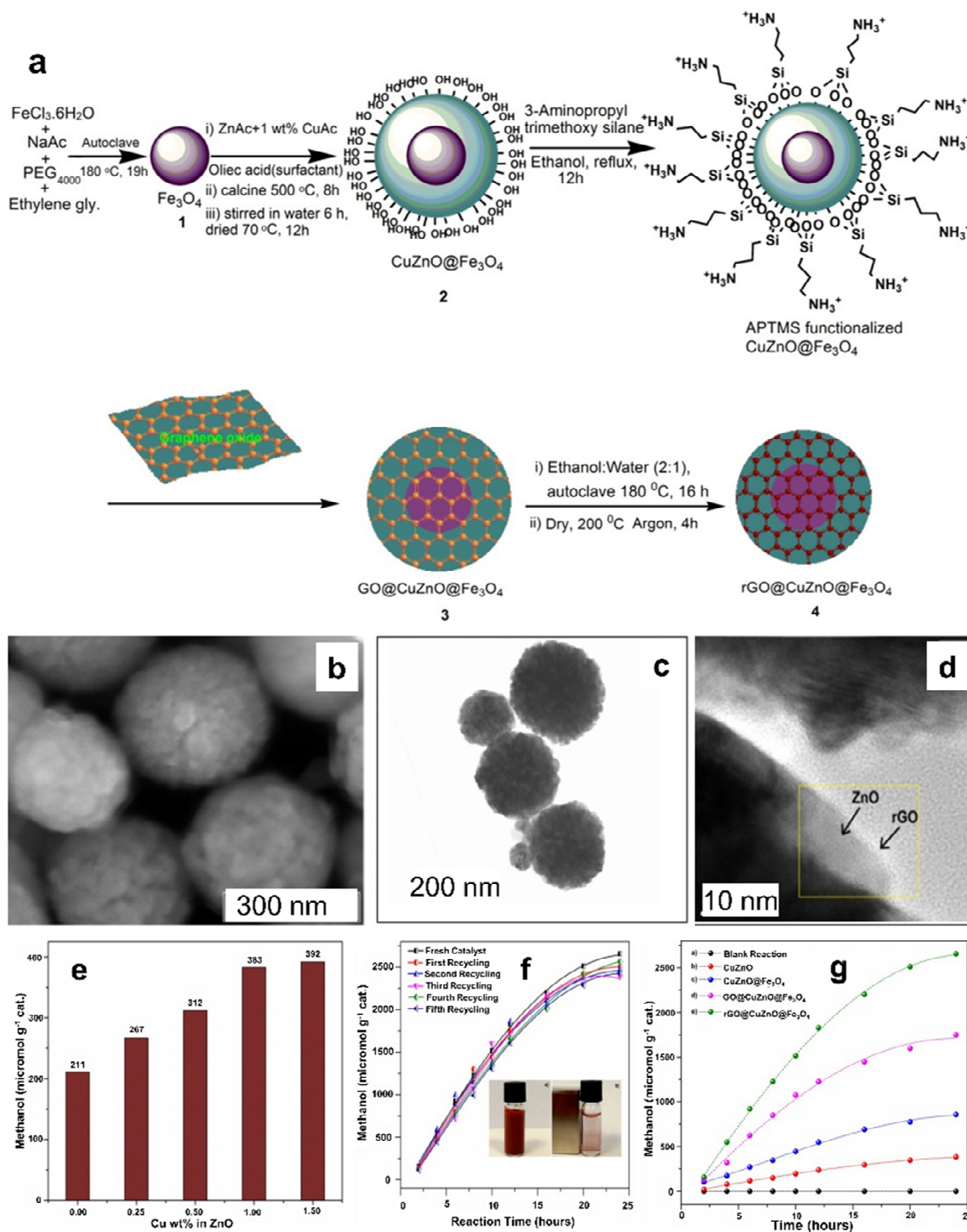


Figure 11. (a) Synthesis of $\text{rGO@CuZnO@Fe}_3\text{O}_4$ catalyst; (b) FE-SEM image; (c) low-resolution TEM(LR-TEM); (d) HR-TEM of $\text{rGO@CuZnO@Fe}_3\text{O}_4$ catalyst; (e) Yield of methanol; (f) Recyclability; (g) Methanol yield using Cu wt% in ZnO. Reproduced from [75] with permission.

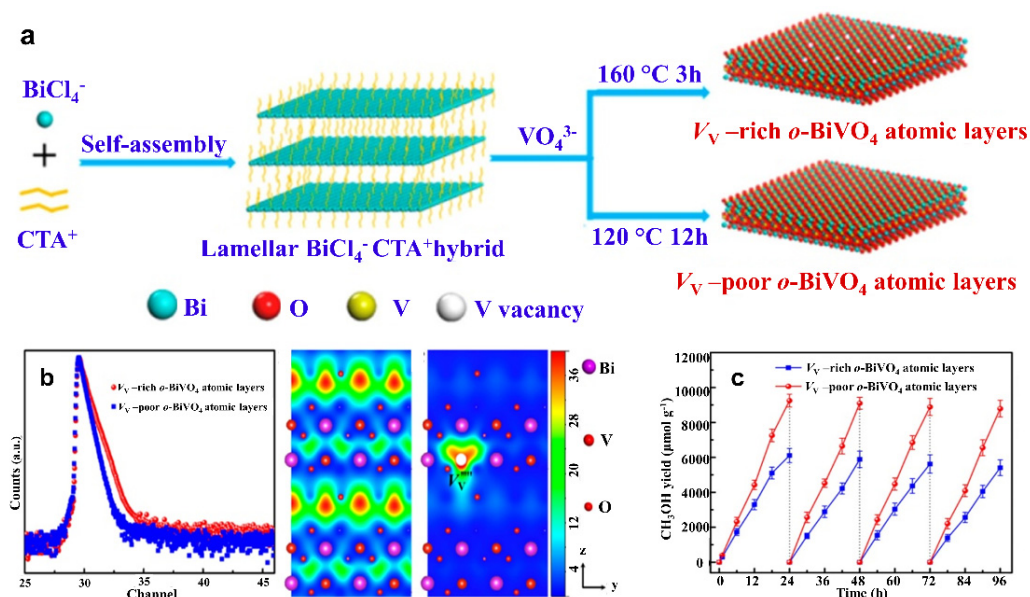


Figure 12. (a) The preparation of (V_v -rich and V_v -poor) atomic layers o-BiVO_4 , (b) Defects characterization positron lifetime spectrum, diagram for trapped positrons; (c) Photocatalytic methanol production (irradiation with visible light). Reproduced from [76] with permission.

Viswanathan et al. synthesized a photocatalyst ($\text{Fe-N}/\text{Na}_{(1-x)}\text{La}_x\text{TaO}_{(3+x)}$) via a hydrothermal method. Using a variety of approaches, researchers evaluated the effect of doping or co-doping LNTO (lantana) with iron (Fe) and nitrogen (N) on the photo-physical properties of catalysts. The dopant iron (Fe-3d) energy level of the orbital was lower than the Ta-5d energy level. The new energy level is under the conduction band. The Fe^{3+} ion (dopant) retains the capacity to capture and de-capture the charge carriers. It can readily capture photogenerated electrons from the CB of NaTaO_3 . A decrease in the PL line intensity suggests that dopants/co-dopants (Fe or N) can reduce recombination, therefore enhancing the charge carrier's lifetime. The enhancement in activity is because of co-doping with N and Fe over lantana (LNTO). The XPS and XRD results show that the Fe^{3+} occupies the Ta_5^+ ions site, La^{3+} ions Na^+ ion sites, and Nitrogen (N) takes O^{2-} sites. N and Fe co-doping in a Ta matrix results in the confining of the bandgap because of the formation of secondary energy levels between the bandgap and the absorption of visible light. The presence of dopants (La^{3+} and Fe^{3+}) in the tantalate (Ta) lattice assures electro-neutrality. The charge trapping and de-trapping of ($\text{Fe}^3/\text{Fe}^{4+}$) ions efficiently decreases the recombination of the charge carrier. The co-doping of LNTO through N and Fe increases the absorption of visible light because of the synergetic effect. It hinders charge carrier recombination and boosts charge transfer interfacial, enhancing photocatalytic CO_2 reduction to CH_3OH in aqueous alkaline media higher than that of pure NaTaO_3 [78].

Kumar et al. developed a Z-scheme heterostructured ($\text{rGO}/\text{InVO}_4/\text{Fe}_2\text{O}_3$) photocatalyst for the reduction of CO_2 to methanol over visible light illumination by the deposition-precipitation method. The existence of a few dark spots over the sheet surface suggested the presence of iron oxide (Fe_2O_3) in the nanocomposites. In Raman spectra, the presence of comparable bands of all constituents at 468, 924, 1329, and 1587 cm^{-1} proved the existence of Fe_2O_3 , InVO_4 , and rGO in the composites. In comparison to Fe_2O_3 and InVO_4 , notably $\text{rGO}/\text{InVO}_4/\text{Fe}_2\text{O}_3$ had a lower PL intensity, indicating less charge recombination and thus greater photocatalytic activity. The XRD pattern indicated the appearance of Fe_2O_3 and InVO_4 into the composite. The photo-induced electron transfer occurred from the CB of Fe_2O_3 into the VB of InVO_4 and further to the CB of InVO_4 over the Z-scheme system for the CO_2 photoreduction. Triethylamine (TEA) was employed as a sacrificial electron donor to achieve methanol yields as high as $16.9\text{ mmol gcat}^{-1}$ employing the Z-scheme-based photocatalyst. The recycling ability of the photocatalyst demonstrated greater stability and

efficient recyclability. The synergistic effect of the ternary rGO/InVO₄/Fe₂O₃ photocatalyst leads to effective separation of charge carriers and charge mobility over the surface of the catalysts, which results in an effective reduction of CO₂ and an enhancement in the yield of methanol [79].

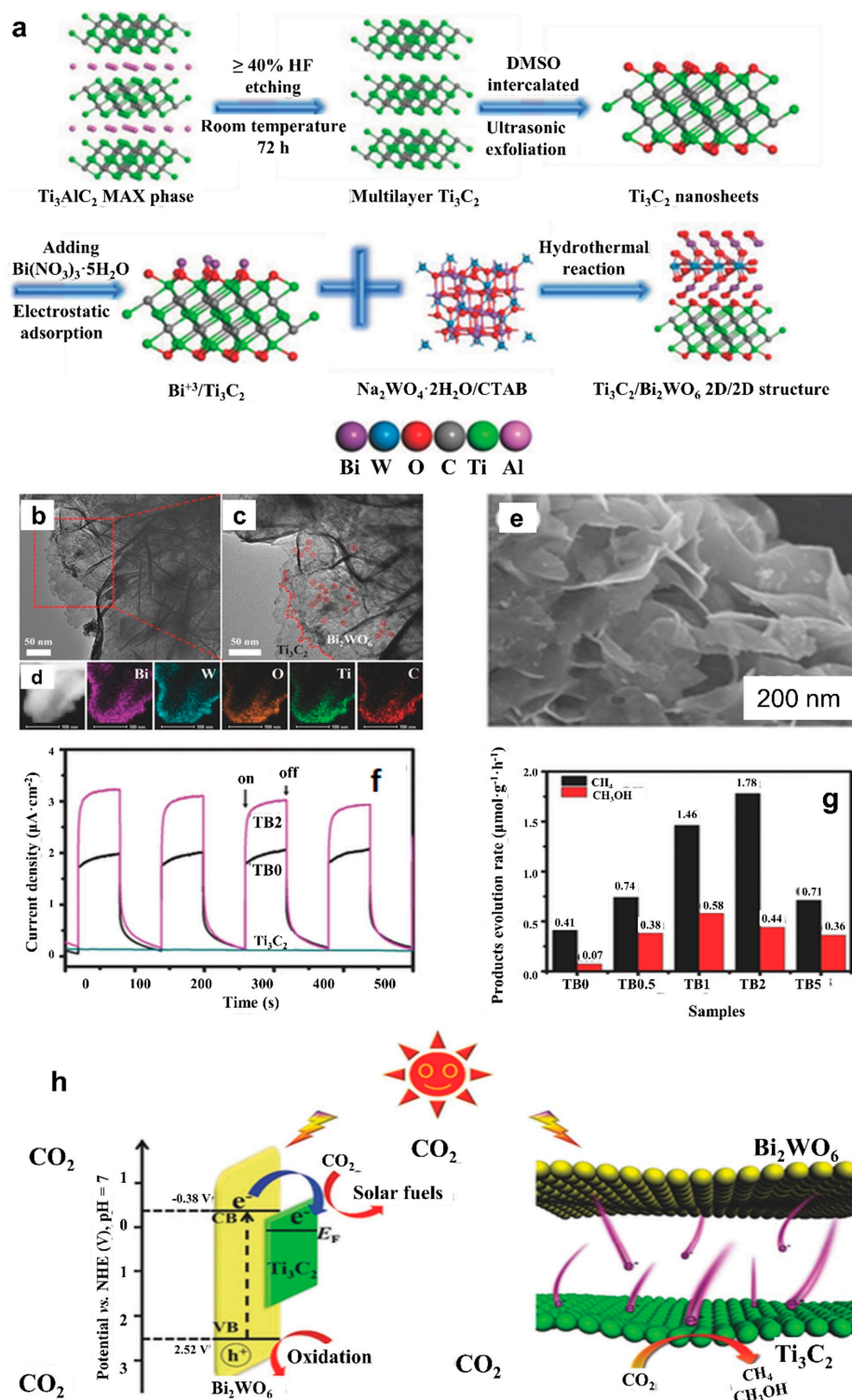


Figure 13. (a) Schematic representation for preparation of ultrathin $\text{Ti}_3\text{C}_2/\text{Bi}_2\text{WO}_6$ nanosheets; (b–d) TEM, enlarged image, elemental mapping; (e) FESEM; (f) Transient photocurrent spectra of the prepared catalyst; (g) Photocatalytic activity; (h) Energy profile diagram of Ti_3C_2 and Bi_2WO_6 and process electron transfer. Reproduced from [77] with permission.

Yan et al. [80] developed a polymorph of indium oxide as a photocatalyst for the formation of CO and CH₃OH. Zhang et al. reported an efficient, highly selective, and stable photocatalyst (In₂O_{3-x}(OH)_y) with a rod-like nano-crystallized structure for hydrogenation of gaseous carbon dioxide to methanol and an evolution rate (0.06 mmol g_{cat}⁻¹ h⁻¹) under solar irradiation [81]. The SEM image showed the rod length of the nanocrystal superstructure to be about 2.6 μm (Figure 14a). The nanoporous nature of the materials produced, made up of nanocrystalline superstructures, has been confirmed by TEM studies (Figure 14b,c). The photocatalytic stability of the In₂O_{3-x}(OH)_y nano-crystallized structure sample was illustrated. The stabilized rate of methanol within the first 15 h led to a significant enhancement in the 16th h optimized at 250 °C in the light for 20 h (Figure 14d). DFT measurements of the energy profile for the production of methanol via CO₂ hydrogenation over In₂O_{3-x}(OH)_y (111) were investigated. An acetal intermediate was formed by adding a hydride (H₂CO₂*). The lowest energy issue was chosen as the probable intermediate (Figure 14e).

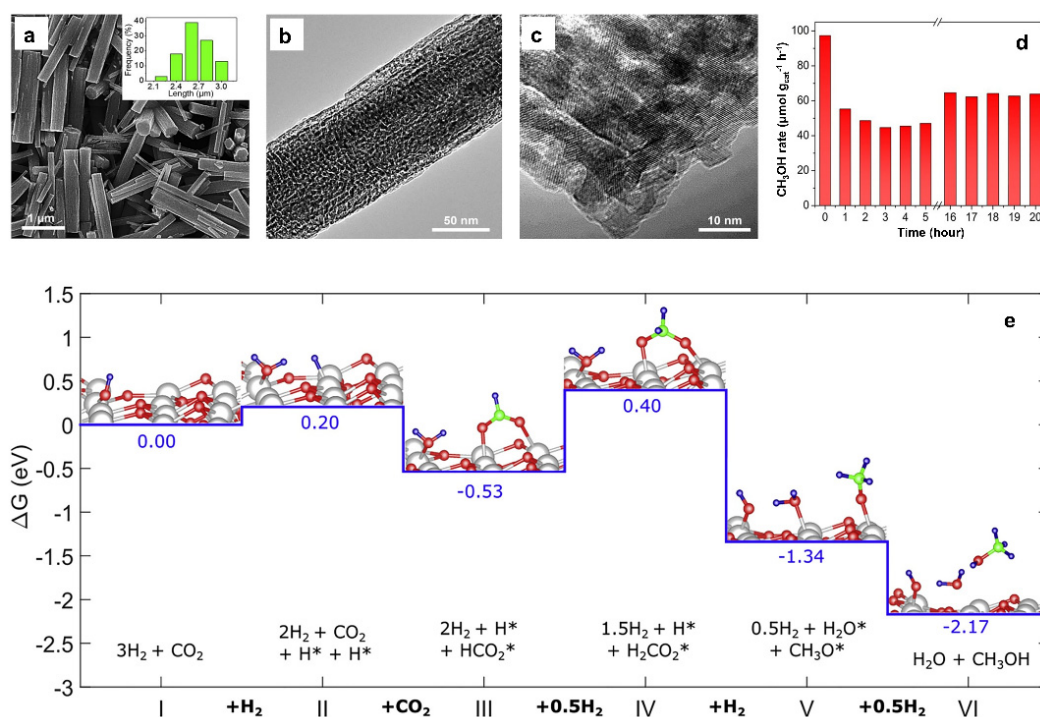


Figure 14. Characterization of In₂O_{3-x}(OH)_y photocatalyst: (a–c) SEM/TEM and HR-TEM images; (d) Stability of catalytic performance; (e) The mechanism for CO₂ hydrogenation into CH₃OH. Reproduced from [81] with permission.

3.3. Photocatalysts Based on Carbon Materials

Carbon-based photocatalysts have become increasingly popular for the reduction of CO₂ because of their excellent physicochemical and electrochemical properties. Several excellent carbon-based supports such as graphene, CNT, carbon dots, graphitic carbon-nitride, and conducting polymers have been employed for several applications over the years. The use of different carbonaceous materials as supports for photocatalysis is highly beneficial, since carbon has fair photocatalytic activity, high surface area, high electrical conductivity, higher dispersion, and visible light absorption capability [82,83].

Gusain et al. synthesized rGO-CuO nanocomposites for CO₂ reduction to methanol over visible light illumination. The deposition of CuO nanorods over rGO enhanced photocatalytic efficiency and produced a higher yield of methanol compared to pure CuO nanorods [84]. In a similar line, Liu et al. prepared cuprous oxide decorated to various morphologies of rGO(Cu₂O/rGO photocatalysts) for CO₂ reduction under visible light.

As-prepared and well characterized rhombic dodecahedral $\text{Cu}_2\text{O}/\text{rGO}$ catalysts exhibited the maximum methanol yield [85].

Yu et al. reported a ternary composite ($\text{Ag}_2\text{CrO}_4/\text{g-C}_3\text{N}_4/\text{GO}$) for the photoreduction of CO_2 to methane and methanol by using silver chromate NPs (photosensitizer) and graphene oxide (cocatalyst) [86]. The dispersion of Ag_2CrO_4 nanoparticles over the surface of the $\text{g-C}_3\text{N}_4$ sheet was investigated through SEM and TEM imaging (Figure 15a,b). The triplet composites displayed an increased conversion of CO_2 with a TOF of 0.30 h^{-1} , which was higher than bare $\text{g-C}_3\text{N}_4$ under sunlight irradiation. The photocatalytic activity was enhanced because of expanded light absorption, greater adsorption of CO_2 , and efficient charge separation. Ag_2CrO_4 nanoparticles can improve the $\text{g-C}_3\text{N}_4$ light absorption, and GO cocatalyst (electron acceptor), besides promoting charge transfer, also provides higher adsorption of CO_2 and catalytic sites. Notably, charge transfer takes place between Ag_2CrO_4 and $\text{g-C}_3\text{N}_4$ via a direct Z-scheme mechanism, which enhances the photocatalytic system's redox ability while promoting charge separation (Figure 15e).

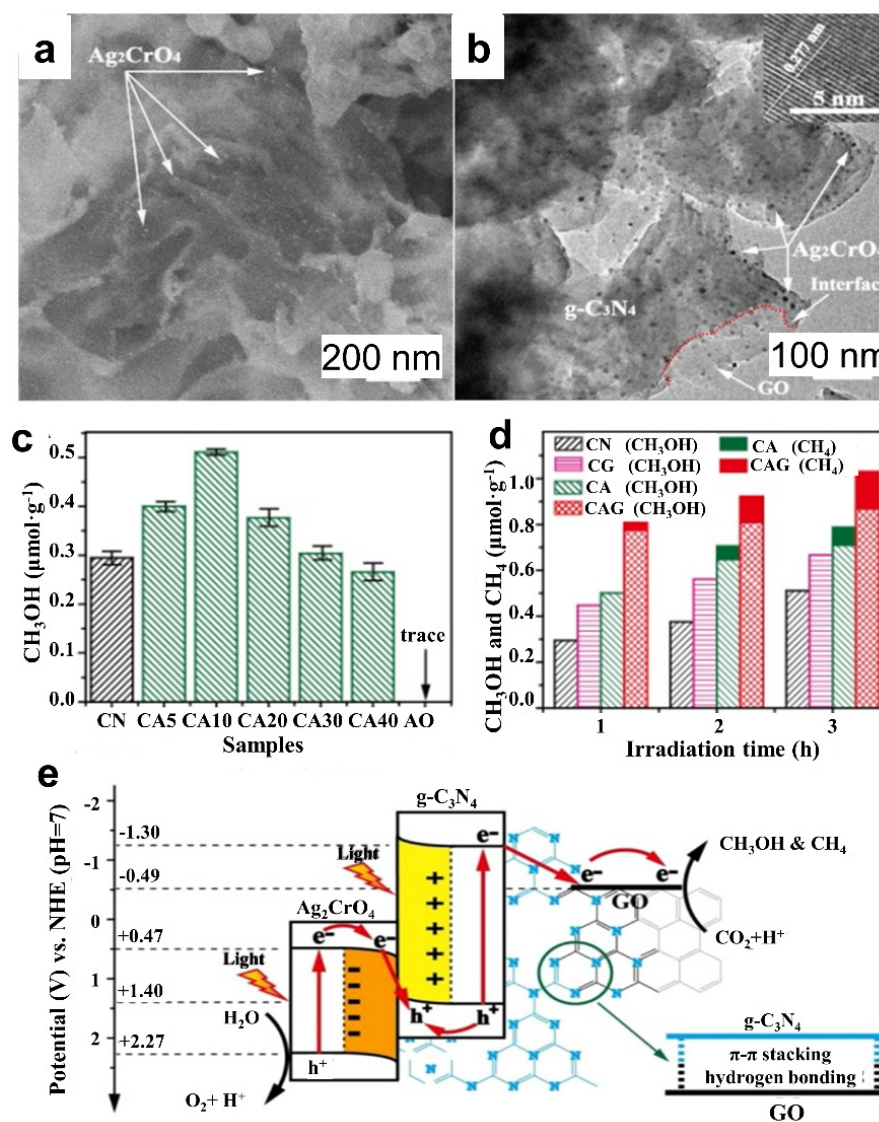


Figure 15. (a,b) Characterization (SEM/TEM images) of the $\text{Ag}_2\text{CrO}_4/\text{g-C}_3\text{N}_4/\text{GO}$ composite photocatalyst; (c) CH_3OH formation of methanol over different samples of CN, under induced sunlight irradiation (1 h); (d) CH_3OH and CH_4 formation over various catalysts; (e) The Z-scheme mechanism for reduction of CO_2 . Reproduced from [86] with permission.

Jain et al. developed a cobalt phthalocyanine embedded over $g\text{-C}_3\text{N}_4$ as a hybrid photocatalyst (denoted as $g\text{-C}_3\text{N}_4/\text{CoPc-COOH}$) for selective reduction of CO_2 into CH_3OH by employing a sacrificial electron donor (triethylamine (TEA) in the presence of visible light (Figure 16a) [87]. The immobilization of the CoPc-COOH complex over the $g\text{-C}_3\text{N}_4$ support was confirmed by HR-TEM (Figure 16b). The resultant $g\text{-C}_3\text{N}_4/\text{CoPc-COOH}$ hybrid provided greatly increased affinity of CO_2 through active Co^{2+} sites, charge separation through the $g\text{-C}_3\text{N}_4$ surface, as well as large surface areas for efficient CO_2 conversion. They have demonstrated and investigated that the hybrid photocatalyst offered a much improved yield of methanol than the reported catalysts. The higher methanol yield over the hybrid photocatalyst was observed after 24 h, employing TEA as an electron contributor (Figure 16c). Notably, the durable interaction between $-\text{COOH}$ with heteroatoms of $g\text{-C}_3\text{N}_4$ support makes a robust hybrid photocatalyst that ultimately inhibits metal leaching during photoreduction.

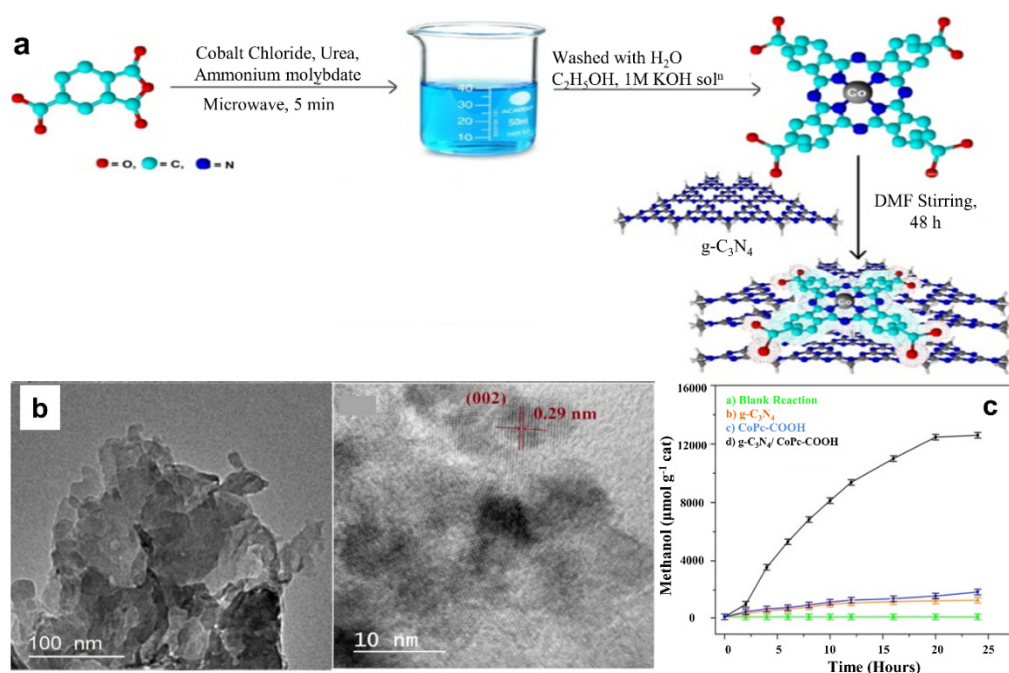


Figure 16. (a) Preparation of $g\text{-C}_3\text{N}_4/\text{CoPc-COOH}$ photocatalyst; (b) HR-TEM images of catalyst; (c) Yield of methanol. Reproduced from [87] with permission.

The Gong group investigated the production of a family of polymeric $\text{C}_3\text{N}_4/\text{CdSe}$ QDs (p-CNCS) with various particle sizes of CdSe for CO_2 photoreduction into methanol, targeting maximum selectivity and activity by the quantum confinement effect [88]. Based on the quantum confinement effect, the energy of the CB electrons was modified to a suitable value, which was deficient for H_2 formation but sufficient for methanol formation, and which enhances activity and selectivity for methanol production from the photocatalytic CO_2 reduction reaction (CO_2RR). CdSe QDs were packed on $p\text{-C}_3\text{N}_4$ via an impregnation method, producing p-CNCS as a photocatalyst (Figure 17b–d). The correlation between the band energy and photocatalytic activity have been discussed. Moreover, the high surface area and appropriate dangling bonds of $p\text{-C}_3\text{N}_4$ (Polymeric carbon nitride nanosheet) provide sufficient loading sites for CdSe quantum dots, allowing a strong interaction between $p\text{-C}_3\text{N}_4$ and CdSe to the heterojunction (Figure 17e,f). The heterojunction within 0D/2D materials could transport photoinduced holes and electrons to CdSe and $p\text{-C}_3\text{N}_4$, enhancing charge separation and increasing CdSe stability.

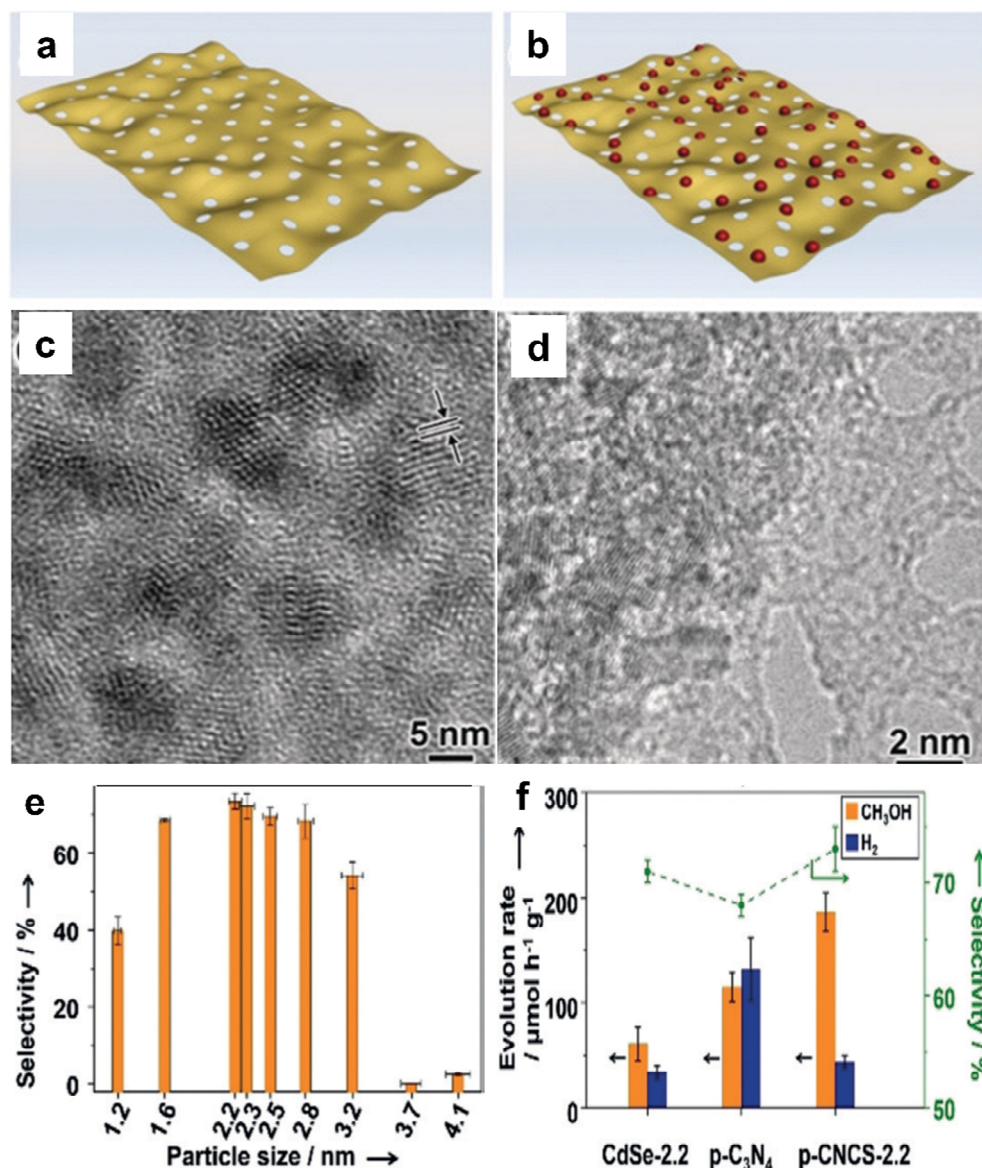


Figure 17. (a) Pattern of p-C₃N₄; (b) Sketch for p-CNCS; (c,d) The HR-TEM images of p-CNCS; (e) Methanol generation selectivity employing with various size of particles; (f) Catalytic performance of as-prepared catalysts. Reproduced from [88] with permission.

Bafaqeer et al. synthesized 2D/2D heterojunction composite catalyst (2D/2D ZnV₂O₆/pCN) via combing ZnV₂O₆ and g-C₃N₄ (protonated -CN) for selective photoreduction of CO₂ with H₂O via the solvothermal method [89]. The HR-TEM was employed to examine the crystalline structure of the pCN merged with ZnV₂O₆ nanosheets (Figure 18b,c). The surface charge conversion with protonation of g-C₃N₄ acts as a moderator and trapped photoexcited electrons. The performances of as-prepared catalysts were studied in gas-phase and liquid photocatalytic methods under light irradiation (UV/visible). The methanol formation rate of the 2D/2D ZnV₂O₆/pCN(100%) composite catalyst was 3742 $\mu\text{mol g-cat}^{-1}$ higher than that of the pure ZnV₂O₆ and pCN catalysts (Figure 18d,e). When bombarded with light, the pCN in the heterostructured photocatalysts functions as a sensitizer, absorbing photons and exciting electron and hole pairs. Photoexcited electrons on pCN might be transported to ZnV₂O₆ CB because the CB edge potential of pCN (1.12 eV) is more negative than that of ZnV₂O₆ (0.87 eV). The protonation of g-C₃N₄ can operate as an excellent acceptor and trap for photoexcited electrons, allowing the photo-induced electrons to be quickly transported to the ZnV₂O₆ and converted to methanol. The photoexcited

electron–hole pairs could be effectively separated in this way. As a result, the created junction between pCN and ZnV_2O_6 in heterostructured photocatalysts reduces electron and hole recombination during the charge carrier transfer process, resulting in improved photocatalytic activity of pCN/ ZnV_2O_6 heterojunctions. In addition to the synergistic effect of ZnV_2O_6 and pCN nanosheet heterojunctions, combining pCN with ZnV_2O_6 resulted in increased activity. Furthermore, the hierarchical structure, rich 2D coupling surfaces, increased interfacial contact, and charge separation could all help to improve photoactivity and product selectivity. The photocatalytic stability of the 2D/2D ZnV_2O_6 /pCN composite catalyst with a moderator was excellent.

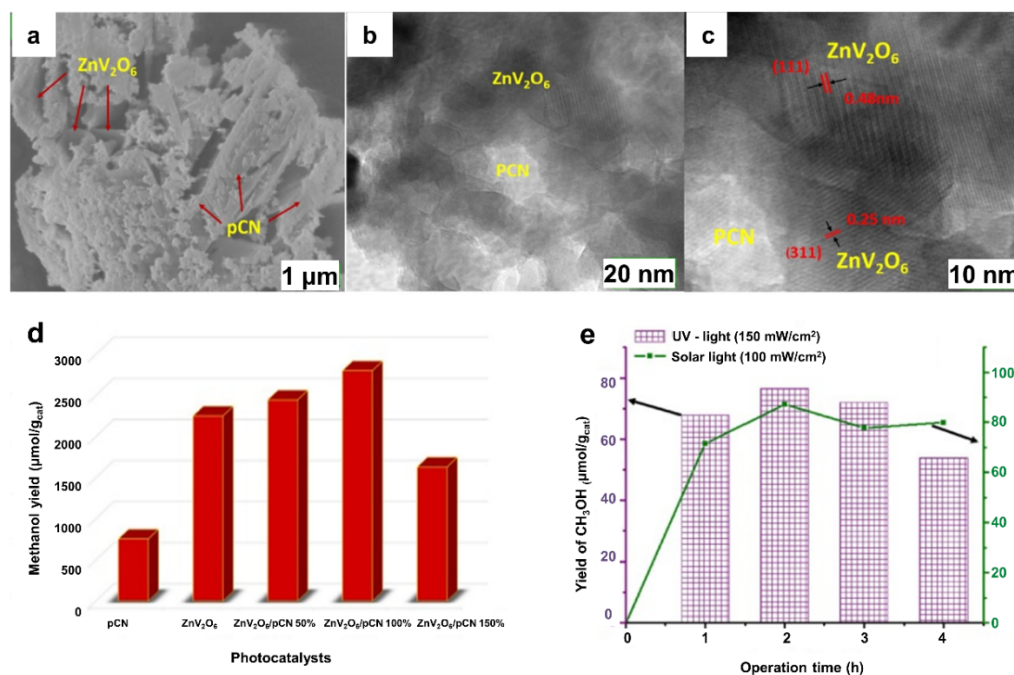


Figure 18. (a) FESEM image of ZnV_2O_6 /pCN (100%) nanosheets; (b,c) TEM and HR-TEM images of ZnV_2O_6 /pCN (100%) nanosheets; (d) yield of CH_3OH over various photocatalysts; (e) yield of CH_3OH for UV and visible light against illumination time. Reproduced from [89] with permission.

Kumar et al. synthesized CNT-TiO₂ photocatalysts for photoreduction of CO₂ and water splitting by joined sonothermal and hydrothermal method [90]. Figure 19a–d shows the effect of CNT on TiO₂ morphology. The (101) plane of anatase TiO₂ (lattice spacing 0.342 nm) is confirmed by HRTEM. The CNT content increases the attachment of spherical TiO₂. The prepared CNT-TiO₂ photocatalysts showed increased photocatalytic activity for the reduction of CO₂ compared to bare TiO₂ in the presence of visible light. As prepared catalysts, the 2.0 CNT-TiO₂ showed better performance for the yield of methanol under UV light (Figure 19g,h). According to a computational study, the binding of CNT to TiO₂ NPs was desirable at (101) surfaces rather than (001) facets (Figure 19e). The photoexcitation of this composite over visible light leads to charge transfer within CNT and TiO₂ and the formation of isolated charge carriers, while UV light excitation leads to charge transfer in all directions from TiO₂ to CNT and CNT to TiO₂ (Figure 19i).

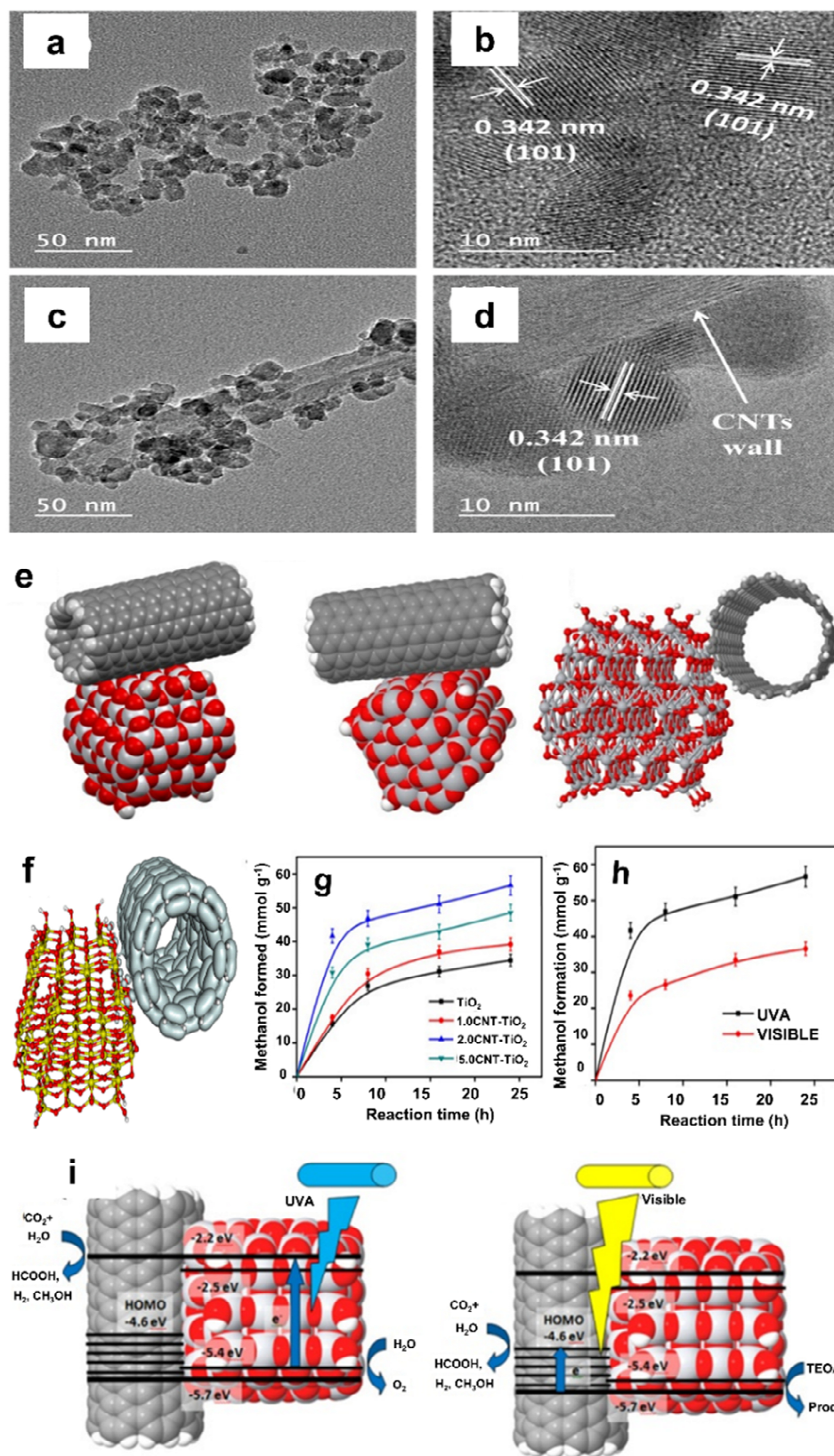


Figure 19. The characterization of (TiO_2 and 2.0 CNT- TiO_2) catalysts (a–d). (e) Structures of CNT- TiO_2 composite; (f) Sketch for CNT- TiO_2 orbitals; (g) Time-dependent profiles for production of methanol; (h) Correlation of methanol production under UVA and visible light; (i) Schematic sketch exhibit formation of product. Reproduced from [90] with permission.

Tang et al. investigated a special variety of CD (carbon-dots) as a hole receiver for mCD/CN composite when produced via the flexible microwave method [38]. The co-residence and morphological information of both mCD and CN structures were investigated through HR-TEM. The as-prepared CN was graphene-like nanosheets, and mCD has a graphitic structure with a featured-spacing of about 0.23 nm (Figure 20a,b). The mCD/CN composite was c.a. 12 times more active than sCD/CN (sonication method) for the conversion of CO₂. Remarkably, the mCD/CN nanocomposite generated methanol and oxygen from H₂O and CO₂ with a selectivity of around 100% methanol (Figure 20d) and an internal quantum efficiency of 2.1% in the visible area, which was validated through isotopic labelling. Furthermore, the unique mCD captured holes from CN (carbon nitride) and hindered methanol adsorption, which resulted in the oxidation of water instead of methanol and the enhancement of the selectivity for reduction of CO₂ to alcohols (Figure 20c).

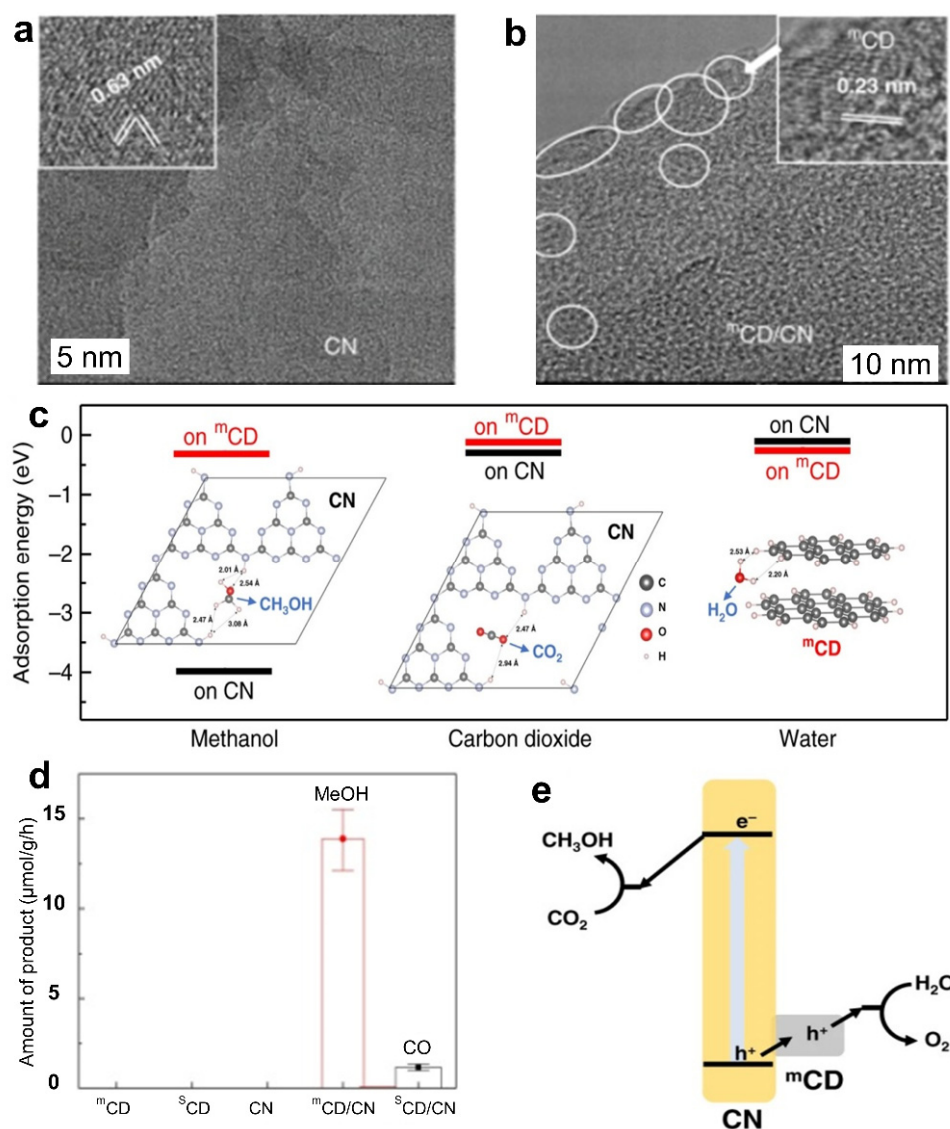


Figure 20. (a) HR-TEM images of CN; (b) HR-TEM images of mCD/CN nanocomposite; (c) The fundamental insights for high methanol selectivity; (d) Yield of methanol; (e) Schematic diagram for photoreduction of CO₂ over the mCD/CN nanocomposites. Reproduced from [38] with permission.

3.4. TiO₂ Based Photocatalysts

Titanium dioxide (TiO₂) is a wide-bandgap semiconductor. In a variety of energy and environmental applications, TiO₂ is employed as a photocatalyst because of its high

stability, efficient photoactivity, low price, and safety for people and the environment. TiO_2 has properties such as nontoxicity, easy availability, chemical stability, and the capability to oxidize in the presence of radiation. TiO_2 -based photocatalysts will be able to solve the main global problems related to pollution of the environment and renewable energy requirements [91,92].

Nogueira et al. reported nanocomposite $\text{TiO}_2/\text{Ti}_4\text{O}_9/\text{Cu}_2\text{O}$ for photocatalytic CO_2 reduction through loading of Cu_2O on TiO_2 -pillared tetratitanate ($\text{K}_2\text{Ti}_4\text{O}_9$) [93]. The structural and compositional characteristics of as-prepared catalysts were investigated through XRD, XPS, and TEM images (Figure 21a–d). The TEM and HR-TEM revealed that the size of the Cu_2O and TiO_2 nanoparticles were approximately 5 and 10 nm, respectively (Figure 21d,e). The enhancement in the photoactivity of the as-prepared photocatalyst was because of the synergistic effect produced by pillaring $\text{K}_2\text{Ti}_4\text{O}_9$ (layered semiconductor) with TiO_2 and the eventual loading of Cu_2O nanoparticles as cocatalyst. The increment in the surface area of the photocatalyst $\text{TiO}_2/\text{Ti}_4\text{O}_9/\text{Cu}_2\text{O}$ was from (25 to $145 \text{ m}^2 \text{ g}^{-1}$) analysed through nitrogen adsorption–desorption isotherms (NADI). The methanol production was double that of the pure $\text{K}_2\text{Ti}_4\text{O}_9$ due to the enhanced activity of the photocatalyst (Figure 21f). Incorporating Cu_2O nanoparticles onto mesoporous solid surfaces extended solar radiation absorption, mobility of electron and charge separation at the surface.

Jiang and co-workers synthesized hybrid carbon@ TiO_2 composite hollow spheres for CO_2 photo-reduction by the simple and benign method of employing colloidal carbon spheres (Figure 22a) [94]. The nanostructure, hollow spherical structure, and elemental mapping of the as-prepared composite were confirmed by FESEM, TEM and STEM analysis (Figure 22b–f). The obtained carbon@ TiO_2 composite nanostructure displayed good photoreduction of CO_2 operation and selectivity over artificial solar light compared to TiO_2 (P25). The methanol generation rate was ($9.1 \mu\text{mol g}^{-1} \text{ h}^{-1}$) greater than pure TiO_2 (Figure 22g). The carbon composition of the carbon@ TiO_2 composites considerably affected photocatalytic activity. The improvement in the photocatalytic performance of the carbon@ TiO_2 photocatalyst was because of enhanced specific surface area ($110 \text{ m}^2 \text{ g}^{-1}$), the CO_2 absorption capacities, and a native photothermal impact near the photocatalyst due to the carbon. According to the electrochemical impedance spectra (EIS), carbon composition could affect the efficiency of charge transfer of carbon@ TiO_2 composites.

Yadav et al. successfully loaded Au nanoparticles on $\text{S}_8\text{-TiO}_2$ ($\text{S}_8\text{-TiO}_2$ (40)-Au photocatalyst) via the sol immobilization method. The as-prepared catalysts employed or CO_2 photoreduction to methanol and HER under visible light irradiation [95]. Sharma et al. developed a nanocomposite photocatalyst $\text{NiO-TiO}_2/\text{ACF}$ via the sol–gel method for photoreduction of CO_2 with H_2O into methanol by immobilization of Ni loaded TiO_2 on initiated carbon fibers (ACFs) under UV and visible light illumination (Figure 23a) [96]. The SEM images of ACF, ACF-TiO_2 and $\text{NiO-TiO}_2/\text{ACF}$ photocatalyst indicated that the even distribution of NiO/TiO_2 nanoparticles was found over the surface of ACF with high crystallinity. The ACF surface was almost clean after pre-treatment with a hierarchical porous structure capable of acting as active sites for adsorption (Figure 23b–d). The yield of methanol over $\text{NiO-TiO}_2/\text{ACF}$ photocatalyst was 986.3 and $755.1 \mu\text{mol g}^{-1}$ under visible light and UV, respectively (Figure 23e). Increasing the photocatalytic activity of Ni-loaded TiO_2 was achieved with the use of the ACF support, which inhibited electron–hole recombination. The ACFs (surface area: $163.9 \text{ m}^2/\text{g}$) and NiO were used to increase CO_2 adsorption capacity and also to alter the electronic absorption properties of TiO_2 . Moreover, NiO co-doped TiO_2 beat the recombination rate issue of electron–hole and induced the formation of Ti^{3+} and oxygen vacancies for CO_2 conversion into CH_3OH over UV/visible light irradiation (Figure 23f).

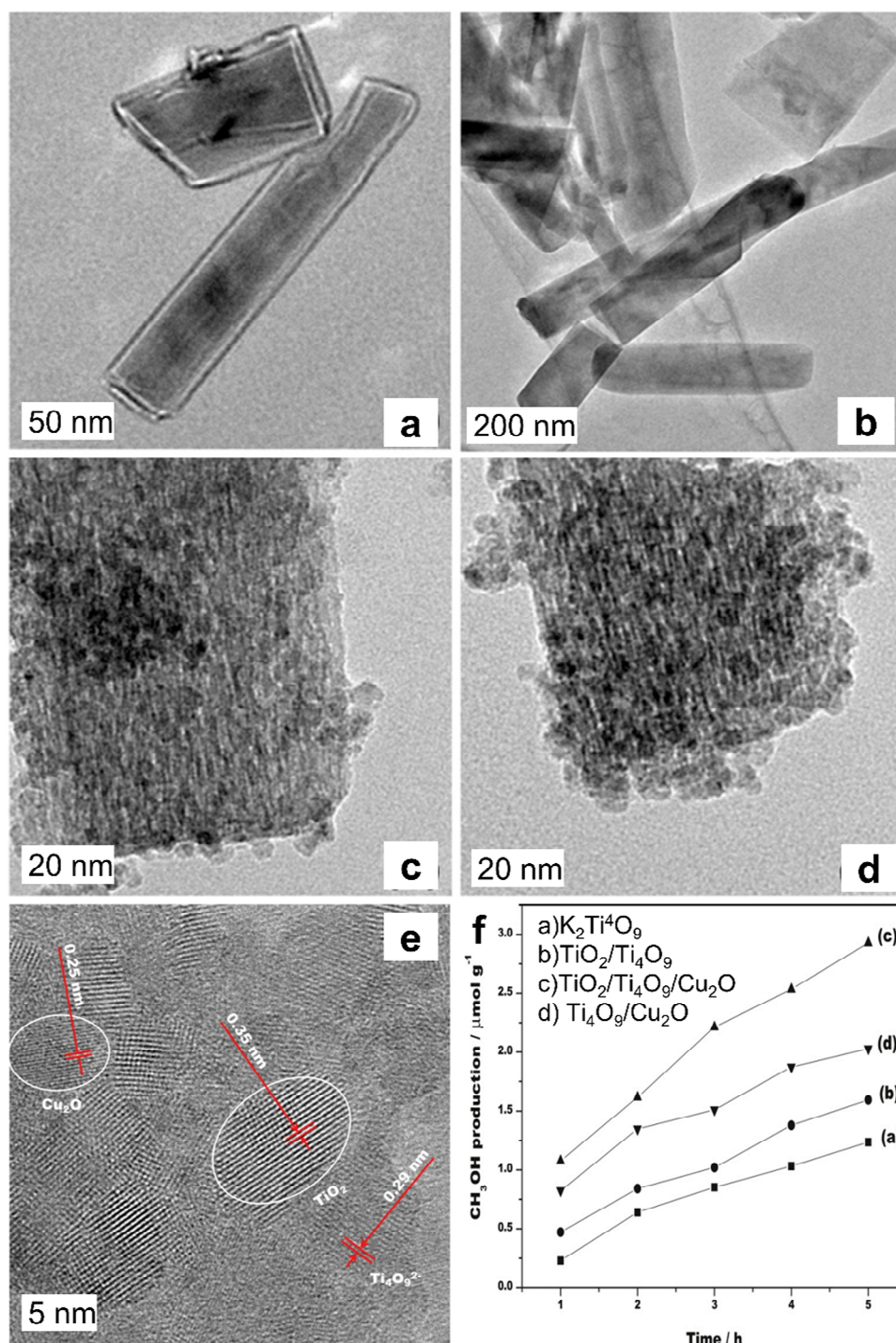


Figure 21. Characterization of the catalysts: (a–d) TEM images of $K_2Ti_4O_9$, $H_2Ti_4O_9$, TiO_2/Ti_4O_9 and $TiO_2/Ti_4O_9/Cu_2O$ photocatalysts; (e) HR-TEM image of $TiO_2/Ti_4O_9/Cu_2O$ photocatalyst; (f) Photocatalytic methanol production over various photocatalysts at 70 °C under artificial solar light. Reproduced from [93] with permission.

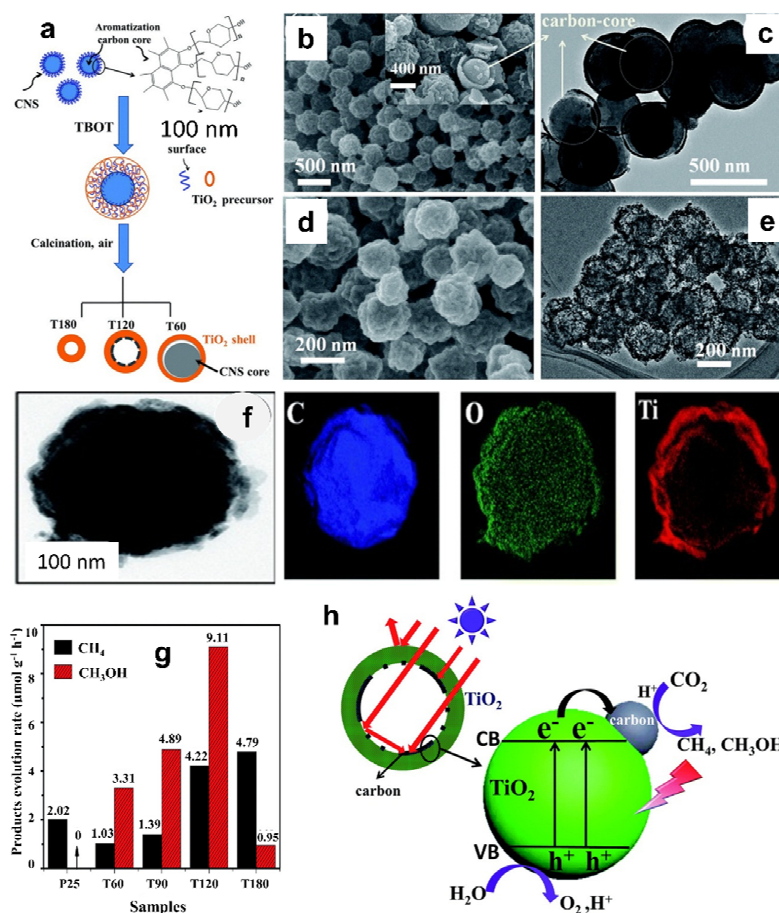


Figure 22. (a) The mechanism for the preparation of carbon@TiO₂ composite hollow structure; (b–e) FESEM and TEM images of samples T60 and T120; (f) STEM image of T60 and comparable elemental mapping images of C, O and Ti; (g) The photocatalytic activity of carbon@TiO₂ composite samples; (h) Photo-excitation process of the carbon@TiO₂ composite. Reproduced from [94] with permission.

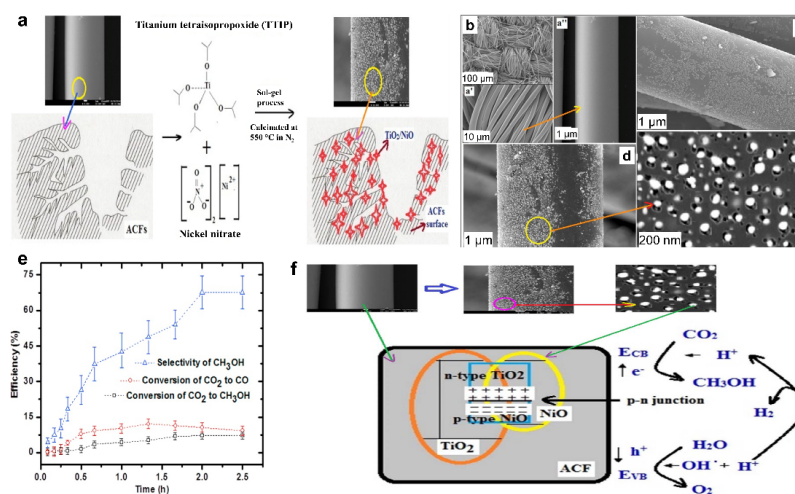


Figure 23. (a) Schematic representation for the preparation of NiO-TiO₂/ACF photocatalyst; SEM images of (b) activated carbon fibers (ACF) and (c) ACF-TiO₂; (d) SEM images of NiO-TiO₂/ACF photocatalyst; (e) Methanol selectivity test for CO₂ conversion to CH₃OH and CO; (f) The mechanism for photocatalytic CO₂ reduction into methanol by using NiO-TiO₂/ACF photocatalyst. Reproduced from [96] with permission.

Xu et al. synthesized hybrid $\text{TiO}_2/\text{Ni}(\text{OH})_2$ photocatalysts for photoreduction of CO_2 by deposition of perpendicularly arranged $\text{Ni}(\text{OH})_2$ nanosheets on the TiO_2 fibers by electrospinning and the wet-chemical precipitation method (Figure 24a) [97]. The FESEM, TEM, and HR-TEM images of $\text{TiO}_2/\text{Ni}(\text{OH})_2$ photocatalyst revealed that the hierarchical nanostructure. The thickness of nanosheets of $\text{Ni}(\text{OH})_2$ was nearly 20 nm and was well deposited on TiO_2 surface (Figure 24b–d). The $\text{TiO}_2/\text{Ni}(\text{OH})_2$ composite nanofiber exhibited unusually enhanced activity of CO_2 photoreduction than the bare TiO_2 fibers. The yield of CH_3OH over this hybrid photocatalyst was increased after loading of 15 wt% $\text{Ni}(\text{OH})_2$ and irradiation time (Figure 24e,f). The $\text{TiO}_2/\text{Ni}(\text{OH})_2$ photocatalyst displayed an increased activity of CO_2 reduction, selectivity, the efficiency of charge separation, and increased the density of the CO_2 on photocatalyst surface due to the existence of $\text{Ni}(\text{OH})_2$ nanosheets as cocatalyst. The clusters of $\text{Ni}(\text{OH})_2/\text{Ni}$ can act as electron sinks and stimulate the photo-generated electron separation from TiO_2 to a cluster of $\text{Ni}(\text{OH})_2/\text{Ni}$ and toward CO_2 molecules, which can play a vital role as active sites and during the photocatalytic process, reducing photo-excited charge carrier recombination (Figure 24g). Later on, modified $\text{TiO}_2/\text{rGO}/\text{CeO}_2$ composite photocatalyst was investigated for CO_2 photoconversion by the ultrasonication method [98].

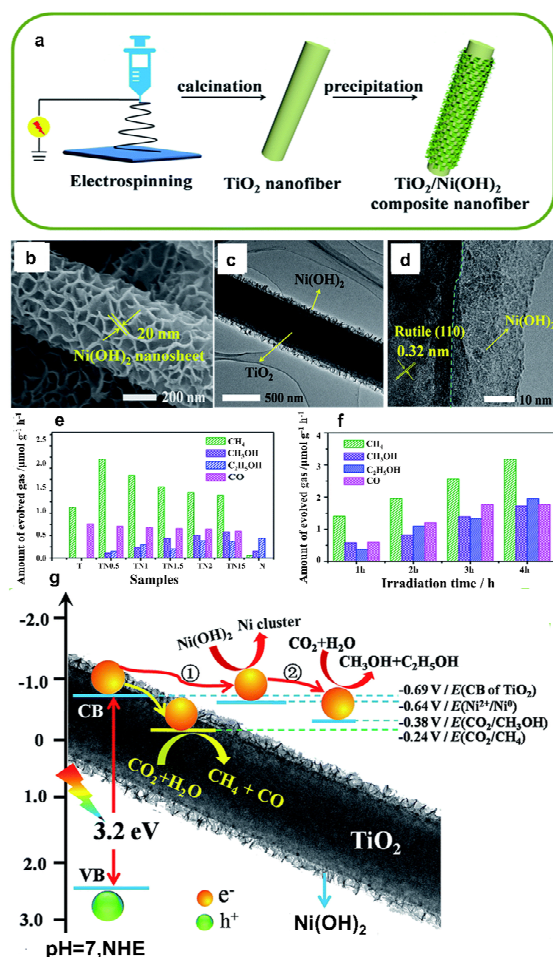


Figure 24. (a) Schematic representation for the synthesis of $\text{TiO}_2/\text{Ni}(\text{OH})_2$ composite; (b–d) FESEM, TEM and HR-TEM images of $\text{TiO}_2/\text{Ni}(\text{OH})_2$ (15 wt% of Ni denoted as sample (TN15) composite nanofibers); (e) Photocatalytic activity of as-prepared catalysts; (f) Time-dependent conversion of CO_2 to products over TN15 ($\text{TiO}_2/\text{Ni}(\text{OH})_2$) photocatalyst; (g) Schematic demonstration of transfer and separation of photogenerated charge carriers with $\text{TiO}_2/\text{Ni}(\text{OH})_2$ nanofibre. Reproduced from [97] with permission.

3.5. Photocatalysts with Plasmonic Properties

Recently, plasmonic photocatalysis has enabled rapid advances in improving the photocatalytic efficiency for CO₂ reduction under irradiation with visible light. It employs precious metal NPs dispersed on semiconductor photocatalysts and has outstanding properties such as localized plasmonic surface resonance (LSPR), which contributes to the strong absorption of visible light and the excitation of active charge carriers. The conduction of electrons on the nanoparticle surface offers plasmonic materials extraordinary optical characteristics. The interaction between free electrons in metal nanoparticles and incident light is known as the plasmonic effect. Plasmonic metal nanoparticles with high light absorptivity have been shown to represent a new class of photocatalysts with features that differ dramatically from those of typical semiconductor photocatalysts. Plasmonic nanoparticles have unique optical, electrical, and thermal properties [99–107]. In this section, we focused on plasmonic photocatalysts for the photoreduction of CO₂ to methanol.

Becerra et al. developed an efficient method for the preparation of plasmonic photocatalyst (Au@ZIF-67) [69]. The decoration of Au NPs over ZIF-67 was investigated for the reduction of CO₂ under irradiation with sunlight. The plasmonic system showed greatly enhanced photocatalytic activity for CO₂ reduction to CH₃OH with excellent selectivity. The plasmonic Au NPs (size 30–40 nm) significantly enhanced the absorption of visible light, increased separation of charge, and contributed to selectivity. This nanocomposite demonstrated the advantages of high specific surface area (SSA) as well as electrochemical properties. An optimal production rate of methanol (~2.5 mmol g⁻¹ h⁻¹) was achieved for the conversion of CO₂. This deposited Au NPs favours both the activity and the selectivity of synthesized plasmonic photocatalyst because of the injection of energetic electrons on the surface of the ZIF-67 derived from the plasmonic response. The localized surface plasmon resonance (LSPR) at the edges of rod- and triangular nanostructures decreases the recombination of electron–hole pairs during the photocatalytic reduction of CO₂. The production of CH₃OH (~2.5 mmol g⁻¹ h⁻¹) and C₂H₅OH (0.5 mmol g⁻¹ h⁻¹) were achieved from Au nanorods and Au nanotriangle, respectively. This Au@ZIF-67 plasmonic system has been significantly improved in terms of photocatalytic activity to reduce CO₂ and improve cost-efficiency. Yadav et al. reported plasmonic photocatalyst (Au/Ti_xSi_{1-x}O₂) for photoreduction of CO₂ employing an LED light source by deposition of plasmonic Au NPs on mesoporous titania with isolated silica (Ti_xSi_{1-x}O₂). Following a DFT study, an excellent adsorption of CO₂ on the surface was observed, which could have been due to the incorporation of silica sites. The methanol production was 1835 μmol g⁻¹ using Au/Ti_xSi_{1-x}O₂ material with 28 mol% Si in titania lattice and 1.0 wt% Au nanoparticle deposition [108].

Ye et al. reported plasmonic catalysts (Cu/ZnO) for photoreduction of CO₂ into methanol that promoted visible light illumination under atmospheric pressure. The rich Cu-ZnO interfaces are recognized as active sites for the production of CH₃OH (Figure 25a). The production rate of methanol rose from 1.38 to 2.13 μmol g⁻¹ min⁻¹, and the noticeable activation energy was reduced from 82.4 to 49.4 kJ mol⁻¹ (Figure 25b). N₂ sorption isotherms specified that the physicochemical characteristics of the decreased Cu/ZnO catalyst were mesoporous in nature (Figure 25c). The mechanism fuses the photo-generated hot electrons onto Cu NPs, and these electrons can transfer to the ZnO via interfaces of metal-support (Figure 25d). The activation of reaction intermediates co-operatively promoted by hot-electrons over Cu and ZnO leads to the photo-promoted synthesis of methanol [109].

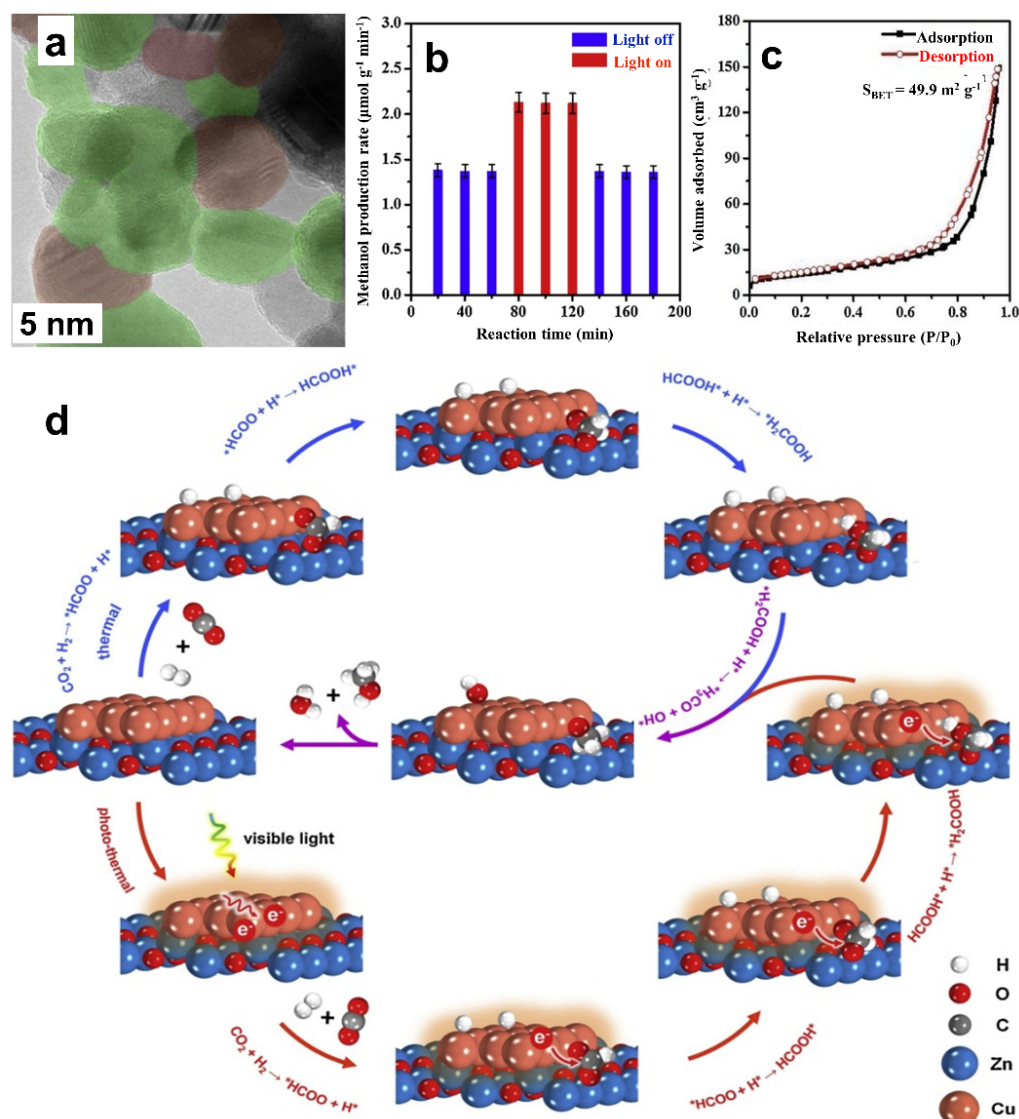


Figure 25. (a) HR-TEM image of Cu/ZnO catalyst; (b) Methanol production; (c) N₂ sorption isotherms; (d) The mechanism of methanol preparation. Reproduced from [109] with permission.

Fan et al. established a plasmonic photocatalyst (Cu/TiO₂) by employing both hydrothermal and microwave-assisted processes [110]. Both Cu NPs and unique TiO₂ film display the properties of light harvesting as per LSPR. The charge carrier recombination was decreased by the deposition of Cu NPs, that were found during fluorescence quenching. The photocatalytic activity of Cu/TiO₂ films was excellent because of charge transfer efficiency and LSPR absorption of Cu NPs. Recently, Wang et al. prepared plasmonic photocatalysts (Ag NPs/ACFs) by deposition of plasmonic Ag NPs over acid-ached carbon fibers (ACFs) coupled with ultrasonication for photoreduction of CO₂ to methanol under visible light irradiation [111].

4. Conclusions and Future Perspectives

In this review, we discussed the recent research advances of photocatalytic CO₂ reduction into methanol. Photocatalysts such as MOFs, mixed-metal oxide, carbon, TiO₂ and plasmonic-based photocatalytic reduction of CO₂ to methanol were systematically summarized. The photocatalytic activity, photo-excited charge transfers and separation efficiency, CO₂ capture capacities, and stability can be enhanced by supporting synthetic procedures, semiconductor, metal, and ligand replacement, and incorporation of photoactive responsive

units. A detailed overview of the catalytic performance of various photocatalysts for CO₂ reduction to methanol would be helpful to researchers. The selectivity and catalytic activity that are mostly directed by the electronic environment of the metals could be attuned by a combination of support, doping of heteroatoms, and employing a system with multiple metals. The photoreduction of CO₂ to valuable chemicals and to fuels has gradually become important because of its efficiency in simultaneously solving global warming and energy crisis problems. Indeed, photoactive materials retain their specific benefits with light-driven CO₂ reduction, and all of these efficient variation strategies will offer directions to the rational design of photocatalysts with improved catalytic performance. It is hoped that this review will play a crucial and interesting role in serving future developments in this important field.

Author Contributions: G.Y.S. collected the complete literature and wrote the complete review. A.S.M. collected some part of the literature and wrote the respective part. M.B.G. edited and revised the draft and supervised the complete work. All authors have read and agreed to the published version of the manuscript.

Funding: This research received no external funding.

Data Availability Statement: Data sharing not applicable.

Acknowledgments: Gajanan Y. Shinde would like to thank the Council of Scientific and Industrial Research (CSIR), Delhi, for financial support through the NET-JRF fellowship.

Conflicts of Interest: The authors declare no conflict of interest.

References

1. Liu, C.; Wang, W.; Liu, B.; Qiao, J.; Lv, L.; Gao, X.; Zhang, X.; Xu, D.; Liu, W.; Liu, J.; et al. Recent Advances in MOF-based Nanocatalysts for Photo-Promoted CO₂ Reduction Applications. *Catalysts* **2019**, *9*, 658. [[CrossRef](#)]
2. Sen, R.; Goepfert, A.; Kar, S.; Prakash, G.K.S. Hydroxide Based Integrated CO₂ Capture from Air and Conversion to Methanol. *J. Am. Chem. Soc.* **2020**, *142*, 4544–4549. [[CrossRef](#)]
3. Singh, A.K.; Montoya, J.H.; Gregoire, J.M.; Persson, K.A. Robust and synthesizable photocatalysts for CO₂ reduction: A data-driven materials discovery. *Nat. Commun.* **2019**, *10*, 443. [[CrossRef](#)]
4. Rath, A.K.; Kmentová, H.; Naldoni, A.; Goswami, A.; Gawande, M.B.; Varma, R.S.; Kment, Š.; Zbořil, R. Significant Enhancement of Photoactivity in Hybrid TiO₂/g-C₃N₄ Nanorod Catalysts Modified with Cu–Ni-Based Nanostructures. *ACS Appl. Nano Mater.* **2018**, *1*, 2526–2535. [[CrossRef](#)]
5. Bharath, G.; Rambabu, K.; Hai, A.; Othman, I.; Ponpandian, N.; Banat, F.; Loke Show, P. Hybrid Pd₅₀-Ru₅₀/MXene (Ti₃C₂T_x) nanocatalyst for effective hydrogenation of CO₂ to methanol toward climate change control. *Chem. Eng. J.* **2021**, *414*, 128869. [[CrossRef](#)]
6. Chen, Y.-H.; Qi, M.-Y.; Li, Y.-H.; Tang, Z.-R.; Wang, T.; Gong, J.; Xu, Y.-J. Activating two-dimensional Ti₃C₂T_x-MXene with single-atom cobalt for efficient CO₂ photoreduction. *Cell Rep. Phys. Sci.* **2021**, *2*, 100371. [[CrossRef](#)]
7. Yang, H.; Wu, Y.; Li, G.; Lin, Q.; Hu, Q.; Zhang, Q.; Liu, J.; He, C. Scalable Production of Efficient Single-Atom Copper Decorated Carbon Membranes for CO₂ Electroreduction to Methanol. *J. Am. Chem. Soc.* **2019**, *141*, 12717–12723. [[CrossRef](#)]
8. Liang, L.; Lei, F.; Gao, S.; Sun, Y.; Jiao, X.; Wu, J.; Qamar, S.; Xie, Y. Single Unit Cell Bismuth Tungstate Layers Realizing Robust Solar CO₂ Reduction to Methanol. *Angew. Chem. Int. Ed.* **2015**, *54*, 13971–13974. [[CrossRef](#)]
9. Rezvani, A.; Abdel-Mageed, A.M.; Ishida, T.; Murayama, T.; Parlinska-Wojtan, M.; Behm, R.J. CO₂ Reduction to Methanol on Au/CeO₂ Catalysts: Mechanistic Insights from Activation/Deactivation and SSITKA Measurements. *ACS Catal.* **2020**, *10*, 3580–3594. [[CrossRef](#)]
10. Zhu, J.; Ciolca, D.; Liu, L.; Parastaev, A.; Kosinov, N.; Hensen, E.J.M. Flame Synthesis of Cu/ZnO–CeO₂ Catalysts: Synergistic Metal–Support Interactions Promote CH₃OH Selectivity in CO₂ Hydrogenation. *ACS Catal.* **2021**, *11*, 4880–4892. [[CrossRef](#)]
11. Yang, D.; Zhu, Q.; Chen, C.; Liu, H.; Liu, Z.; Zhao, Z.; Zhang, X.; Liu, S.; Han, B. Selective electroreduction of carbon dioxide to methanol on copper selenide nanocatalysts. *Nat. Commun.* **2019**, *10*, 677. [[CrossRef](#)]
12. Sharma, R.K.; Yadav, S.; Dutta, S.; Kale, H.B.; Warkad, I.R.; Zbořil, R.; Varma, R.S.; Gawande, M.B. Silver nanomaterials: Synthesis and (electro/photo) catalytic applications. *Chem. Soc. Rev.* **2021**, *50*, 11293–11380. [[CrossRef](#)] [[PubMed](#)]
13. Al Jitan, S.; Palmisano, G.; Garlisi, C. Synthesis and Surface Modification of TiO₂-Based Photocatalysts for the Conversion of CO₂. *Catalysts* **2020**, *10*, 227. [[CrossRef](#)]
14. Yang, X.; Wang, D. Photocatalysis: From Fundamental Principles to Materials and Applications. *ACS Appl. Energy Mater.* **2018**, *1*, 6657–6693. [[CrossRef](#)]
15. Kumar, S.; Gawande, M.B.; Kopp, J.; Kment, S.; Varma, R.S.; Zboril, R. P- and F-co-doped Carbon Nitride Nanocatalysts for Photocatalytic CO₂ Reduction and Thermocatalytic Furanics Synthesis from Sugars. *ChemSusChem* **2020**, *13*, 5231–5238. [[CrossRef](#)]

16. Sharma, P.; Kumar, S.; Tomanec, O.; Petr, M.; Zhu Chen, J.; Miller, J.T.; Varma, R.S.; Gawande, M.B.; Zbořil, R. Carbon Nitride-Based Ruthenium Single Atom Photocatalyst for CO₂ Reduction to Methanol. *Small* **2021**, *17*, 2006478. [[CrossRef](#)]
17. Goyal, S.; Shaharun, M.S.; Jayabal, G.S.; Kait, C.F.; Abdullah, B.; Wei, L.J. Photocatalytic Reduction of CO₂ to Methanol Using a Copper-Zirconia Imidazolate Framework. *Catalysts* **2021**, *11*, 346. [[CrossRef](#)]
18. Izadpanah Ostad, M.; Niknam Shahrak, M.; Galli, F. Photocatalytic carbon dioxide reduction to methanol catalyzed by ZnO, Pt, Au, and Cu nanoparticles decorated zeolitic imidazolate framework-8. *J. CO₂ Util.* **2021**, *43*, 101373. [[CrossRef](#)]
19. Wu, Y.A.; McNulty, I.; Liu, C.; Lau, K.C.; Liu, Q.; Paulikas, A.P.; Sun, C.-J.; Cai, Z.; Guest, J.R.; Ren, Y.; et al. Facet-dependent active sites of a single Cu₂O particle photocatalyst for CO₂ reduction to methanol. *Nat. Energy* **2019**, *4*, 957–968. [[CrossRef](#)]
20. Zeng, Z.; Yan, Y.; Chen, J.; Zan, P.; Tian, Q.; Chen, P. Boosting the Photocatalytic Ability of Cu₂O Nanowires for CO₂ Conversion by MXene Quantum Dots. *Adv. Funct. Mater.* **2019**, *29*, 1806500. [[CrossRef](#)]
21. Adekoya, D.O.; Tahir, M.; Amin, N.A.S. g-C₃N₄/(Cu/TiO₂) nanocomposite for enhanced photoreduction of CO₂ to CH₃OH and HCOOH under UV/visible light. *J. CO₂ Util.* **2017**, *18*, 261–274. [[CrossRef](#)]
22. Gao, G.; Jiao, Y.; Waclawik, E.R.; Du, A. Single Atom (Pd/Pt) Supported on Graphitic Carbon Nitride as an Efficient Photocatalyst for Visible-Light Reduction of Carbon Dioxide. *J. Am. Chem. Soc.* **2016**, *138*, 6292–6297. [[CrossRef](#)]
23. Fu, J.; Zhu, B.; Jiang, C.; Cheng, B.; You, W.; Yu, J. Hierarchical Porous O-Doped g-C₃N₄ with Enhanced Photocatalytic CO₂ Reduction Activity. *Small* **2017**, *13*, 1603938. [[CrossRef](#)]
24. Albo, J.; Qadir, M.I.; Samperi, M.; Fernandes, J.A.; de Pedro, I.; Dupont, J. Use of an optofluidic microreactor and Cu nanoparticles synthesized in ionic liquid and embedded in TiO₂ for an efficient photoreduction of CO₂ to methanol. *Chem. Eng.* **2021**, *404*, 126643. [[CrossRef](#)]
25. Billo, T.; Fu, F.Y.; Raghunath, P.; Shown, I.; Chen, W.F.; Lien, H.T.; Shen, T.H.; Lee, J.F.; Chan, T.S.; Huang, K.Y.; et al. Ni-Nanocluster Modified Black TiO₂ with Dual Active Sites for Selective Photocatalytic CO₂ Reduction. *Small* **2018**, *14*, 1702928. [[CrossRef](#)]
26. Rechberger, F.; Niederberger, M. Translucent nanoparticle-based aerogel monoliths as 3-dimensional photocatalysts for the selective photoreduction of CO₂ to methanol in a continuous flow reactor. *Mater. Horiz.* **2017**, *4*, 1115–1121. [[CrossRef](#)]
27. Wu, J.; Feng, Y.; Logan, B.E.; Dai, C.; Han, X.; Li, D.; Liu, J. Preparation of Al–O-Linked Porous-g-C₃N₄/TiO₂-Nanotube Z-Scheme Composites for Efficient Photocatalytic CO₂ Conversion and 2,4-Dichlorophenol Decomposition and Mechanism. *ACS Sustain. Chem. Eng.* **2019**, *7*, 15289–15296. [[CrossRef](#)]
28. Zeng, G.; Qiu, J.; Li, Z.; Pavaskar, P.; Cronin, S.B. CO₂ Reduction to Methanol on TiO₂-Passivated GaP Photocatalysts. *ACS Catal.* **2014**, *4*, 3512–3516. [[CrossRef](#)]
29. Guo, H.; Wan, S.; Wang, Y.; Ma, W.; Zhong, Q.; Ding, J. Enhanced photocatalytic CO₂ reduction over direct Z-scheme NiTiO₃/g-C₃N₄ nanocomposite promoted by efficient interfacial charge transfer. *Chem. Eng. J.* **2021**, *412*, 128646. [[CrossRef](#)]
30. Nor, N.U.M.; Amin, N.A.S. Glucose precursor carbon-doped TiO₂ heterojunctions for enhanced efficiency in photocatalytic reduction of carbon dioxide to methanol. *J. CO₂ Util.* **2019**, *33*, 372–383. [[CrossRef](#)]
31. Liu, J.-Y.; Gong, X.-Q.; Alexandrova, A.N. Mechanism of CO₂ Photocatalytic Reduction to Methane and Methanol on Defected Anatase TiO₂ (101): A Density Functional Theory Study. *J. Phys. Chem. C* **2019**, *123*, 3505–3511. [[CrossRef](#)]
32. Bahadori, E.; Tripodi, A.; Villa, A.; Pirola, C.; Prati, L.; Ramis, G.; Dimitratos, N.; Wang, D.; Rossetti, I. High pressure CO₂ photoreduction using Au/TiO₂: Unravelling the effect of co-catalysts and of titania polymorphs. *Catal. Sci. Technol.* **2019**, *9*, 2253–2265. [[CrossRef](#)]
33. Olowoyo, J.O.; Saini, U.; Kumar, M.; Valdés, H.; Singh, H.; Omorogie, M.O.; Babalola, J.O.; Vorontsov, A.V.; Kumar, U.; Smirniotis, P.G. Reduced graphene oxide/NH₂-MIL-125(Ti) composite: Selective CO₂ photoreduction to methanol under visible light and computational insights into charge separation. *J. CO₂ Util.* **2020**, *42*, 101300. [[CrossRef](#)]
34. Liu, Y.; Yang, Y.; Sun, Q.; Wang, Z.; Huang, B.; Dai, Y.; Qin, X.; Zhang, X. Chemical adsorption enhanced CO₂ capture and photoreduction over a copper porphyrin based metal organic framework. *ACS Appl. Mater. Interfaces* **2013**, *5*, 7654–7658. [[CrossRef](#)] [[PubMed](#)]
35. Liu, Q.; Low, Z.-X.; Li, L.; Razmjou, A.; Wang, K.; Yao, J.; Wang, H. ZIF-8/Zn₂GeO₄ nanorods with an enhanced CO₂ adsorption property in an aqueous medium for photocatalytic synthesis of liquid fuel. *J. Mater. Chem. A* **2013**, *1*, 11563–11569. [[CrossRef](#)]
36. Alhaddad, M.; Shawky, A. Pt-decorated ZnMn₂O₄ nanorods for effective photocatalytic reduction of CO₂ into methanol under visible light. *Ceram. Int.* **2021**, *47*, 9763–9770. [[CrossRef](#)]
37. Wang, Y.; Liu, H.; Pan, Q.; Ding, N.; Yang, C.; Zhang, Z.; Jia, C.; Li, Z.; Liu, J.; Zhao, Y. Construction of Thiazolo[5,4-d]thiazole-based Two-Dimensional Network for Efficient Photocatalytic CO₂ Reduction. *ACS Appl. Mater. Interfaces* **2020**, *12*, 46483–46489. [[CrossRef](#)] [[PubMed](#)]
38. Wang, Y.; Liu, X.; Han, X.; Godin, R.; Chen, J.; Zhou, W.; Jiang, C.; Thompson, J.F.; Mustafa, K.B.; Shevlin, S.A.; et al. Unique hole-accepting carbon-dots promoting selective carbon dioxide reduction nearly 100% to methanol by pure water. *Nat. Commun.* **2020**, *11*, 2531. [[CrossRef](#)]
39. Chen, K.; Zhao, X.; Zhang, X.-J.; Zhang, W.-S.; Wu, Z.-F.; Wang, H.-Y.; Han, D.-X.; Niu, L. Enhanced photocatalytic CO₂ reduction by constructing an In₂O₃–CuO heterojunction with CuO as a cocatalyst. *Catal. Sci. Technol.* **2021**, *11*, 2713–2717. [[CrossRef](#)]
40. McFarlan, A. Techno-economic assessment of pathways for electricity generation in northern remote communities in Canada using methanol and dimethyl ether to replace diesel. *Renew. Sustain. Energy Rev.* **2018**, *90*, 863–876. [[CrossRef](#)]
41. Bunyakiat, K.; Makmee, S.; Sawangkeaw, R.; Ngamprasertsith, S. Continuous Production of Biodiesel via Transesterification from Vegetable Oils in Supercritical Methanol. *Energy Fuels* **2006**, *20*, 812–817. [[CrossRef](#)]

42. Williams, R.H.; Larson, E.D.; Katofsky, R.E.; Chen, J. Methanol and hydrogen from biomass for transportation. *Energy Sustain. Dev.* **1995**, *1*, 18–34. [[CrossRef](#)]
43. Bowker, M. Methanol Synthesis from CO₂ Hydrogenation. *ChemCatChem* **2019**, *11*, 4238–4246. [[CrossRef](#)]
44. Din, I.U.; Shaharun, M.S.; Alotaibi, M.A.; Alharthi, A.I.; Naeem, A. Recent developments on heterogeneous catalytic CO₂ reduction to methanol. *J. CO₂ Util.* **2019**, *34*, 20–33. [[CrossRef](#)]
45. Yang, Z.; Qi, Y.; Wang, F.; Han, Z.; Jiang, Y.; Han, H.; Liu, J.; Zhang, X.; Ong, W.J. State-of-the-art advancements in photo-assisted CO₂ hydrogenation: Recent progress in catalyst development and reaction mechanisms. *J. Mater. Chem. A* **2020**, *8*, 24868–24894. [[CrossRef](#)]
46. Li, X.; Yu, J.; Jaroniec, M.; Chen, X. Cocatalysts for Selective Photoreduction of CO₂ into Solar Fuels. *Chem. Rev.* **2019**, *119*, 3962–4179. [[CrossRef](#)]
47. Adekoya, D.; Tahir, M.; Amin, N.A.S. Recent trends in photocatalytic materials for reduction of carbon dioxide to methanol. *Renew. Sustain. Energy Rev.* **2019**, *116*, 109389. [[CrossRef](#)]
48. Fu, Z.; Yang, Q.; Liu, Z.; Chen, F.; Yao, F.; Xie, T.; Zhong, Y.; Wang, D.; Li, J.; Li, X.; et al. Photocatalytic conversion of carbon dioxide: From products to design the catalysts. *J. CO₂ Util.* **2019**, *34*, 63–73. [[CrossRef](#)]
49. Li, D.; Kassymova, M.; Cai, X.; Zang, S.-Q.; Jiang, H.-L. Photocatalytic CO₂ reduction over metal-organic framework-based materials. *Coord. Chem. Rev.* **2020**, *412*, 213262. [[CrossRef](#)]
50. Lei, Z.; Xue, Y.; Chen, W.; Qiu, W.; Zhang, Y.; Horike, S.; Tang, L. MOFs-Based Heterogeneous Catalysts: New Opportunities for Energy-Related CO₂ Conversion. *Adv. Energy Mater.* **2018**, *8*, 1801587. [[CrossRef](#)]
51. Chen, Y.; Jia, G.; Hu, Y.; Fan, G.; Tsang, Y.H.; Li, Z.; Zou, Z. Two-dimensional nanomaterials for photocatalytic CO₂ reduction to solar fuels. *Sustain. Energy Fuels* **2017**, *1*, 1875–1898. [[CrossRef](#)]
52. Wang, C.; Sun, Z.; Zheng, Y.; Hu, Y.H. Recent progress in visible light photocatalytic conversion of carbon dioxide. *J. Mater. Chem. A* **2019**, *7*, 865–887. [[CrossRef](#)]
53. Zhong, J.; Yang, X.; Wu, Z.; Liang, B.; Huang, Y.; Zhang, T. State of the art and perspectives in heterogeneous catalysis of CO₂ hydrogenation to methanol. *Chem. Soc. Rev.* **2020**, *49*, 1385–1413. [[CrossRef](#)] [[PubMed](#)]
54. Maina, J.W.; Pozo-Gonzalo, C.; Kong, L.; Schütz, J.; Hill, M.; Dumée, L.F. Metal organic framework based catalysts for CO₂ conversion. *Mater. Horiz.* **2017**, *4*, 345–361. [[CrossRef](#)]
55. Su, Y.; Zhang, Z.; Liu, H.; Wang, Y. Cd_{0.2}Zn_{0.8}S@UiO-66-NH₂ nanocomposites as efficient and stable visible-light-driven photocatalyst for H₂ evolution and CO₂ reduction. *Appl. Catal. B Environ.* **2017**, *200*, 448–457. [[CrossRef](#)]
56. Zhang, G.; Wang, Z.; Wu, J. Construction of a Z-scheme heterojunction for high-efficiency visible-light-driven photocatalytic CO₂ reduction. *Nanoscale* **2021**, *13*, 4359–4389. [[CrossRef](#)] [[PubMed](#)]
57. Xu, Q.; Zhang, L.; Yu, J.; Wageh, S.; Al-Ghamdi, A.A.; Jaroniec, M. Direct Z-scheme photocatalysts: Principles, synthesis, and applications. *Mater. Today* **2018**, *21*, 1042–1063. [[CrossRef](#)]
58. Meng, J.; Chen, Q.; Lu, J.; Liu, H. Z-Scheme Photocatalytic CO₂ Reduction on a Heterostructure of Oxygen-Defective ZnO/Reduced Graphene Oxide/UiO-66-NH₂ under Visible Light. *ACS Appl. Mater. Interfaces* **2019**, *11*, 550–562. [[CrossRef](#)]
59. Wang, G.; He, C.-T.; Huang, R.; Mao, J.; Wang, D.; Li, Y. Photoinduction of Cu Single Atoms Decorated on UiO-66-NH₂ for Enhanced Photocatalytic Reduction of CO₂ to Liquid Fuels. *J. Am. Chem. Soc.* **2020**, *142*, 19339–19345. [[CrossRef](#)]
60. Liu, S.; Chen, F.; Li, S.; Peng, X.; Xiong, Y. Enhanced photocatalytic conversion of greenhouse gas CO₂ into solar fuels over g-C₃N₄ nanotubes with decorated transparent ZIF-8 nanoclusters. *Appl. Catal. B Environ.* **2017**, *211*, 1–10. [[CrossRef](#)]
61. Maina, J.W.; Schutz, J.A.; Grundy, L.; Des Ligneris, E.; Yi, Z.; Kong, L.; Pozo-Gonzalo, C.; Ionescu, M.; Dumee, L.F. Inorganic Nanoparticles/Metal Organic Framework Hybrid Membrane Reactors for Efficient Photocatalytic Conversion of CO₂. *ACS Appl. Mater. Interfaces* **2017**, *9*, 35010–35017. [[CrossRef](#)] [[PubMed](#)]
62. Cardoso, J.C.; Stulp, S.; de Brito, J.F.; Flor, J.B.S.; Frem, R.C.G.; Zanoni, M.V.B. MOFs based on ZIF-8 deposited on TiO₂ nanotubes increase the surface adsorption of CO₂ and its photoelectrocatalytic reduction to alcohols in aqueous media. *Appl. Catal. B Environ.* **2018**, *225*, 563–573. [[CrossRef](#)]
63. An, B.; Zhang, J.; Cheng, K.; Ji, P.; Wang, C.; Lin, W. Confinement of Ultrasmall Cu/ZnOx Nanoparticles in Metal–Organic Frameworks for Selective Methanol Synthesis from Catalytic Hydrogenation of CO₂. *J. Am. Chem. Soc.* **2017**, *139*, 3834–3840. [[CrossRef](#)] [[PubMed](#)]
64. Li, N.; Liu, X.; Zhou, J.; Chen, W.; Liu, M. Encapsulating CuO quantum dots in MIL-125(Ti) coupled with g-C₃N₄ for efficient photocatalytic CO₂ reduction. *Chem. Eng. J.* **2020**, *399*, 125782. [[CrossRef](#)]
65. Li, J.; Luo, D.; Yang, C.; He, S.; Chen, S.; Lin, J.; Zhu, L.; Li, X. Copper(II) imidazolate frameworks as highly efficient photocatalysts for reduction of CO₂ into methanol under visible light irradiation. *J. Solid State Chem.* **2013**, *203*, 154–159. [[CrossRef](#)]
66. Chen, S.; Yu, J.; Zhang, J. Enhanced photocatalytic CO₂ reduction activity of MOF-derived ZnO/NiO porous hollow spheres. *J. CO₂ Util.* **2018**, *24*, 548–554. [[CrossRef](#)]
67. Goyal, S.; Shaharun, M.; Kait, C.; Abdullah, B.; Ameen, M. Photoreduction of Carbon Dioxide to Methanol over Copper Based Zeolitic Imidazolate Framework-8: A New Generation Photocatalyst. *Catalysts* **2018**, *8*, 581. [[CrossRef](#)]
68. Nadeem, S.; Mumtaz, A.; Mumtaz, M.; Abdul Mutalib, M.I.; Shaharun, M.S.; Abdullah, B. Visible light driven CO₂ reduction to methanol by Cu-porphyrin impregnated mesoporous Ti-MCM-48. *J. Mol. Liq.* **2018**, *272*, 656–667. [[CrossRef](#)]

69. Becerra, J.; Nguyen, D.-T.; Gopalakrishnan, V.-N.; Do, T.-O. Plasmonic Au Nanoparticles Incorporated in the Zeolitic Imidazolate Framework (ZIF-67) for the Efficient Sunlight-Driven Photoreduction of CO₂. *ACS Appl. Energy Mater.* **2020**, *3*, 7659–7665. [CrossRef]
70. Burange, A.S.; Gawande, M.B. Role of Mixed Metal Oxides in Heterogeneous Catalysis. In *Encyclopedia of Inorganic and Bioinorganic Chemistry*; Wiley: Hoboken, NJ, USA, 2016; pp. 1–19.
71. Gawande, M.B.; Pandey, R.K.; Jayaram, R.V. Role of mixed metal oxides in catalysis science—Versatile applications in organic synthesis. *Catal. Sci. Technol.* **2012**, *2*, 1113–1125. [CrossRef]
72. Thompson, W.A.; Olivo, A.; Zanardo, D.; Cruciani, G.; Menegazzo, F.; Signoretto, M.; Maroto-Valer, M.M. Systematic study of TiO₂/ZnO mixed metal oxides for CO₂ photoreduction. *RSC Adv.* **2019**, *9*, 21660–21666. [CrossRef]
73. Singhal, N.; Goyal, R.; Kumar, U. Visible-Light-Assisted Photocatalytic CO₂ Reduction over InTaO₄: Selective Methanol Formation. *Energy Fuels* **2017**, *31*, 12434–12438. [CrossRef]
74. Wang, Z.; Jiao, X.; Chen, D.; Li, C.; Zhang, M. Porous Copper/Zinc Bimetallic Oxides Derived from MOFs for Efficient Photocatalytic Reduction of CO₂ to Methanol. *Catalysts* **2020**, *10*, 1127. [CrossRef]
75. Kumar, P.; Joshi, C.; Barras, A.; Sieber, B.; Addad, A.; Boussekey, L.; Szunerits, S.; Boukherroub, R.; Jain, S.L. Core-shell structured reduced graphene oxide wrapped magnetically separable rGO@CuZnO@Fe₃O₄ microspheres as superior photocatalyst for CO₂ reduction under visible light. *Appl. Catal. B Environ.* **2017**, *205*, 654–665. [CrossRef]
76. Gao, S.; Gu, B.; Jiao, X.; Sun, Y.; Zu, X.; Yang, F.; Zhu, W.; Wang, C.; Feng, Z.; Ye, B.; et al. Highly Efficient and Exceptionally Durable CO₂ Photoreduction to Methanol over Freestanding Defective Single-Unit-Cell Bismuth Vanadate Layers. *J. Am. Chem. Soc.* **2017**, *139*, 3438–3445. [CrossRef]
77. Cao, S.; Shen, B.; Tong, T.; Fu, J.; Yu, J. 2D/2D Heterojunction of Ultrathin MXene/Bi₂WO₆ Nanosheets for Improved Photocatalytic CO₂ Reduction. *Adv. Funct. Mater.* **2018**, *28*, 1800136. [CrossRef]
78. Jeyalakshmi, V.; Mahalakshmy, R.; Ramesh, K.; Rao, P.V.C.; Choudary, N.V.; Thirunavukkarasu, K.; Krishnamurthy, K.R.; Viswanathan, B. Metal oxides as photo catalysts: Modified sodium tantalate as catalyst for photo reduction of carbon dioxide. *Mol. Catal.* **2018**, *451*, 105–113. [CrossRef]
79. Kumar, A.; Prajapati, P.K.; Pal, U.; Jain, S.L. Ternary rGO/InVO₄/Fe₂O₃ Z-Scheme Heterostructured Photocatalyst for CO₂ Reduction under Visible Light Irradiation. *ACS Sustain. Chem. Eng.* **2018**, *6*, 8201–8211. [CrossRef]
80. Yan, T.; Wang, L.; Liang, Y.; Makaremi, M.; Wood, T.E.; Dai, Y.; Huang, B.; Jelle, A.A.; Dong, Y.; Ozin, G.A. Polymorph selection towards photocatalytic gaseous CO₂ hydrogenation. *Nat. Commun.* **2019**, *10*, 2521. [CrossRef]
81. Wang, L.; Ghossoub, M.; Wang, H.; Shao, Y.; Sun, W.; Tountas, A.A.; Wood, T.E.; Li, H.; Loh, J.Y.Y.; Dong, Y.; et al. Photocatalytic Hydrogenation of Carbon Dioxide with High Selectivity to Methanol at Atmospheric Pressure. *Joule* **2018**, *2*, 1369–1381. [CrossRef]
82. Kandy, M.M. Carbon-based photocatalysts for enhanced photocatalytic reduction of CO₂ to solar fuels. *Sustain. Energy Fuels* **2020**, *4*, 469–484. [CrossRef]
83. Lin, J.; Tian, W.; Zhang, H.; Duan, X.; Sun, H.; Wang, S. Graphitic Carbon Nitride-Based Z-Scheme Structure for Photocatalytic CO₂ Reduction. *Energy Fuels* **2021**, *35*, 7–24. [CrossRef]
84. Gusain, R.; Kumar, P.; Sharma, O.P.; Jain, S.L.; Khatri, O.P. Reduced graphene oxide–CuO nanocomposites for photocatalytic conversion of CO₂ into methanol under visible light irradiation. *Appl. Catal. B Environ.* **2016**, *181*, 352–362. [CrossRef]
85. Liu, S.-H.; Lu, J.-S.; Pu, Y.-C.; Fan, H.-C. Enhanced photoreduction of CO₂ into methanol by facet-dependent Cu₂O/reduce graphene oxide. *J. CO₂ Util.* **2019**, *33*, 171–178. [CrossRef]
86. Xu, D.; Cheng, B.; Wang, W.; Jiang, C.; Yu, J. Ag₂CrO₄/g-C₃N₄/graphene oxide ternary nanocomposite Z-scheme photocatalyst with enhanced CO₂ reduction activity. *Appl. Catal. B Environ.* **2018**, *231*, 368–380. [CrossRef]
87. Kumar, A.; Prajapati, P.K.; Aathira, M.S.; Bansiwala, A.; Boukherroub, R.; Jain, S.L. Highly improved photoreduction of carbon dioxide to methanol using cobalt phthalocyanine grafted to graphitic carbon nitride as photocatalyst under visible light irradiation. *J. Colloid Interface Sci.* **2019**, *543*, 201–213. [CrossRef]
88. Li, A.; Wang, T.; Li, C.; Huang, Z.; Luo, Z.; Gong, J. Adjusting the Reduction Potential of Electrons by Quantum Confinement for Selective Photoreduction of CO₂ to Methanol. *Angew. Chem. Int. Ed.* **2019**, *58*, 3804–3808. [CrossRef]
89. Bafaqeer, A.; Tahir, M.; Amin, N.A.S. Well-designed ZnV₂O₆/g-C₃N₄ 2D/2D nanosheets heterojunction with faster charges separation via pCN as mediator towards enhanced photocatalytic reduction of CO₂ to fuels. *Appl. Catal. B Environ.* **2019**, *242*, 312–326. [CrossRef]
90. Olowoyo, J.O.; Kumar, M.; Jain, S.L.; Babalola, J.O.; Vorontsov, A.V.; Kumar, U. Insights into Reinforced Photocatalytic Activity of the CNT-TiO₂ Nanocomposite for CO₂ Reduction and Water Splitting. *J. Phys. Chem. C* **2019**, *123*, 367–378. [CrossRef]
91. Xu, H.; Ouyang, S.; Liu, L.; Reunchan, P.; Umezawa, N.; Ye, J. Recent advances in TiO₂-based photocatalysis. *J. Mater. Chem. A* **2014**, *2*, 12642–12661. [CrossRef]
92. Kou, J.; Lu, C.; Wang, J.; Chen, Y.; Xu, Z.; Varma, R.S. Selectivity Enhancement in Heterogeneous Photocatalytic Transformations. *Chem. Rev.* **2017**, *117*, 1445–1514. [CrossRef] [PubMed]
93. Alves Melo Júnior, M.; Morais, A.; Nogueira, A.F. Boosting the solar-light-driven methanol production through CO₂ photoreduction by loading Cu₂O on TiO₂-pillared K₂Ti₄O₉. *Microporous Mesoporous Mater.* **2016**, *234*, 1–11. [CrossRef]
94. Wang, W.; Xu, D.; Cheng, B.; Yu, J.; Jiang, C. Hybrid carbon@TiO₂ hollow spheres with enhanced photocatalytic CO₂ reduction activity. *J. Mater. Chem. A* **2017**, *5*, 5020–5029. [CrossRef]

95. Yadav, R.; Sinha, A.K. Titania Cowrapped α -Sulfur Composite as a Visible Light Active Photocatalyst for Hydrogen Evolution Using in Situ Methanol from CO_2 as a Sacrificial Agent. *ACS Sustain. Chem. Eng.* **2017**, *5*, 6736–6745. [[CrossRef](#)]
96. Sharma, A.; Lee, B.-K. Photocatalytic reduction of carbon dioxide to methanol using nickel-loaded TiO_2 supported on activated carbon fiber. *Catal. Today* **2017**, *298*, 158–167. [[CrossRef](#)]
97. Meng, A.; Wu, S.; Cheng, B.; Yu, J.; Xu, J. Hierarchical $\text{TiO}_2/\text{Ni}(\text{OH})_2$ composite fibers with enhanced photocatalytic CO_2 reduction performance. *J. Mater. Chem. A* **2018**, *6*, 4729–4736. [[CrossRef](#)]
98. Seeharaj, P.; Kongmun, P.; Paiplo, P.; Prakobmit, S.; Sriwong, C.; Kim-Lohsoontorn, P.; Vittayakorn, N. Ultrasonically-assisted surface modified $\text{TiO}_2/\text{rGO}/\text{CeO}_2$ heterojunction photocatalysts for conversion of CO_2 to methanol and ethanol. *Ultrason. Sonochem.* **2019**, *58*, 104657. [[CrossRef](#)]
99. Zhu, Q.; Xuan, Y.; Zhang, K.; Chang, K. Enhancing photocatalytic CO_2 reduction performance of g- C_3N_4 -based catalysts with non-noble plasmonic nanoparticles. *Appl. Catal. B Environ.* **2021**, *297*, 120440. [[CrossRef](#)]
100. Collado, L.; Reynal, A.; Coronado, J.M.; Serrano, D.P.; Durrant, J.R.; de la Peña O’Shea, V.A. Effect of Au surface plasmon nanoparticles on the selective CO_2 photoreduction to CH_4 . *Appl. Catal. B Environ.* **2015**, *178*, 177–185. [[CrossRef](#)]
101. Tahir, M.; Tahir, B.; Amin, N.A.S. Synergistic effect in plasmonic Au/Ag alloy NPs co-coated TiO_2 NWs toward visible-light enhanced CO_2 photoreduction to fuels. *Appl. Catal. B Environ.* **2017**, *204*, 548–560. [[CrossRef](#)]
102. Mahyoub, S.A.; Hezang, A.; Qaraah, F.A.; Namratha, K.; Nayan, M.B.; Drmash, Q.A.; Ponnamma, D.; Byrappa, K. Surface Plasmonic Resonance and Z-Scheme Charge Transport Synergy in Three-Dimensional Flower-like Ag- CeO_2 -ZnO Heterostructures for Highly Improved Photocatalytic CO_2 Reduction. *ACS Appl. Energy Mater.* **2021**, *4*, 3544–3554. [[CrossRef](#)]
103. Zhang, X.; Ke, X.; Yao, J. Recent development of plasmon-mediated photocatalysts and their potential in selectivity regulation. *J. Mater. Chem. A* **2018**, *6*, 1941–1966. [[CrossRef](#)]
104. Vu, N.N.; Kaliaguine, S.; Do, T.O. Plasmonic Photocatalysts for Sunlight-Driven Reduction of CO_2 : Details, Developments, and Perspectives. *ChemSusChem* **2020**, *13*, 3967–3991. [[CrossRef](#)]
105. Jun, H.; Choi, S.; Yang, M.Y.; Nam, Y.S. A ruthenium-based plasmonic hybrid photocatalyst for aqueous carbon dioxide conversion with a high reaction rate and selectivity. *J. Mater. Chem. A* **2019**, *7*, 17254–17260. [[CrossRef](#)]
106. Verma, R.; Belgamwar, R.; Polshettiwar, V. Plasmonic Photocatalysis for CO_2 Conversion to Chemicals and Fuels. *ACS Mater. Lett.* **2021**, *3*, 574–598. [[CrossRef](#)]
107. Becerra, J.; Gopalakrishnan, V.N.; Quach, T.-A.; Do, T.-O. Enhancing CO_2 photoreduction over ZIF-based reticular materials by morphology control of Au plasmonic nanoparticles. *Sustain. Energy Fuels* **2022**. [[CrossRef](#)]
108. Yadav, R.; Amoli, V.; Singh, J.; Tripathi, M.K.; Bhanja, P.; Bhaumik, A.; Sinha, A.K. Plasmonic gold deposited on mesoporous $\text{Ti}_x\text{Si}_{1-x}\text{O}_2$ with isolated silica in lattice: An excellent photocatalyst for photocatalytic conversion of CO_2 into methanol under visible light irradiation. *J. CO₂ Util.* **2018**, *27*, 11–21. [[CrossRef](#)]
109. Wang, Z.-J.; Song, H.; Pang, H.; Ning, Y.; Dao, T.D.; Wang, Z.; Chen, H.; Weng, Y.; Fu, Q.; Nagao, T.; et al. Photo-assisted methanol synthesis via CO_2 reduction under ambient pressure over plasmonic Cu/ZnO catalysts. *Appl. Catal. B Environ.* **2019**, *250*, 10–16. [[CrossRef](#)]
110. Liu, E.; Qi, L.; Bian, J.; Chen, Y.; Hu, X.; Fan, J.; Liu, H.; Zhu, C.; Wang, Q. A facile strategy to fabricate plasmonic Cu modified TiO_2 nano-flower films for photocatalytic reduction of CO_2 to methanol. *Mater. Res. Bull.* **2015**, *68*, 203–209. [[CrossRef](#)]
111. Wang, R.; Ding, J.; Zhong, Q.; Hu, J.; Guo, H.; Liu, Q. Plasmonic Ag Nanoparticles Decorated Acid-Aching Carbon Fibers for Enhanced Photocatalytic Reduction of CO_2 into CH_3OH Under Visible-Light Irradiation. *Catal. Lett.* **2021**, *151*, 3079–3088. [[CrossRef](#)]